

Gravitational waves from first-order phase transitions in LISA: reconstruction pipeline and physics interpretation

Chiara Caprini,^{a,b} Ryusuke Jinno,^c Marek Lewicki,^{d,1} Eric Madge,^{e,2,*}
Marco Merchand,^{f,g} Germano Nardini,^{h,3} Mauro Pieroni,^{b,4} Alberto Roper Pol,^a
Ville Vaskonen^{i,j,k}

(For the LISA Cosmology Working Group)

^a*Département de Physique Théorique and Center for Astroparticle Physics, Université de Genève, Quai E. Ansermet 24, CH-1211 Genève 4, Switzerland*

^b*Theoretical Physics Department, CERN, 1211 Geneva 23, Switzerland*

^c*Research Center for the Early Universe (RESCEU), University of Tokyo, Hongo 7-3-1, Bunkyo-ku, Tokyo 113-003, Japan*

^d*Faculty of Physics, University of Warsaw, ul. Pasteura 5, 02-093 Warsaw, Poland*

^e*Department of Particle Physics and Astrophysics, Weizmann Institute of Science, Herzl Street 234, Rehovot, 7610001, Israel*

^f*Department of Physics, KTH Royal Institute of Technology, SE-10691 Stockholm, Sweden*

^g*The Oskar Klein Centre for Cosmoparticle Physics, AlbaNova University Centre, SE-10691 Stockholm, Sweden*

^h*Department of Mathematics and Physics, University of Stavanger, NO-4036 Stavanger, Norway*

ⁱ*Dipartimento di Fisica e Astronomia, Università degli Studi di Padova, Via Marzolo 8, 35131 Padova, Italy*

^j*Istituto Nazionale di Fisica Nucleare, Sezione di Padova, Via Marzolo 8, 35131 Padova, Italy*

^k*Keemilise ja bioloogilise füüsika instituut, Rävala pst. 10, 10143 Tallinn, Estonia*

E-mail: chiara.caprini@unige.ch,
ryusuke.jinno@resceu.s.u-tokyo.ac.jp, marek.lewicki@fuw.edu.pl,
eric.madgimentel@uam.es, marcomm@kth.se, germano.nardini@uis.no,
mauro.pieroni@cern.ch, alberto.roperpol@unige.ch,
ville.vaskonen@pd.infn.it

¹Project coordinator: marek.lewicki@fuw.edu.pl

²Corresponding author: eric.madgimentel@uam.es

*Now at *Instituto de Física Teórica UAM-CSIC, Universidad Autónoma de Madrid, C/ Nicolás Cabrera 13-15, Cantoblanco, Madrid 28049, Spain*

³Project coordinator: germano.nardini@uis.no

⁴Corresponding author: mauro.pieroni@cern.ch

ABSTRACT: We develop a tool for the analysis of stochastic gravitational wave backgrounds from cosmological first-order phase transitions with LISA: we initiate a template databank for these signals, prototype their searches, and forecast their reconstruction. The templates encompass the gravitational wave signals sourced by bubble collisions, sound waves and turbulence. Accounting for Galactic and extra-Galactic foregrounds, we forecast the region of the parameter space that LISA will reconstruct with better than $\sim 10\%$ accuracy, if certain experimental and theoretical uncertainties are solved by the time LISA flies. We illustrate the accuracy with which LISA can reconstruct the parameters on a few benchmark signals, both in terms of the template parameters and the phase transition ones. To show the impact of the forecasts on physics beyond the Standard Model, we map the reconstructed benchmark measurements into the parameter spaces of the singlet extension of the Standard Model and of the classically conformal invariant $U(1)_{B-L}$ model.

Contents

1	Introduction	2
2	SGWB templates for first-order phase transitions	4
2.1	Template I: broken power law for bubble collisions and highly relativistic fluid shells	5
2.2	Template II: double broken power law	7
2.2.1	Sound waves	9
2.2.2	Magnetohydrodynamic turbulence	10
3	Parameter reach and reconstruction	13
3.1	LISA measurement channels	13
3.2	Data in each channel	14
3.3	Injected (and reconstructed) noises and signals	16
3.4	Data generation and analysis	17
4	Reconstruction of the geometric parameters	19
4.1	Broken power law	19
4.2	Double broken power law	22
4.3	Synergy with other gravitational wave observatories	23
5	Reconstruction of the thermodynamic parameters	24
6	Interpretation in terms of fundamental particle physics models	33
6.1	Gauge singlet extension with \mathbb{Z}_2 symmetry	35
6.2	Classically conformal $U(1)_{B-L}$ model	37
7	Conclusions	40

1 Introduction

Cosmology and astrophysics are currently at the dawn of a new golden age thanks to the discovery of gravitational waves (GWs), which started with the first direct detections by the LIGO/Virgo/KAGRA (LVK) collaboration [1–9] of GWs emitted by black hole and neutron star mergers in the late Universe. Recently, Pulsar Timing Array (PTA) collaborations have presented strong evidence for the presence of a stochastic GW background (SGWB) at nano-Hertz frequencies [10–13]. The front-runner candidate for the source of this signal is associated with binaries of supermassive black holes, colliding relatively recently in cosmological terms [14–16], and interacting with their environment. However, at this stage, it is also possible that this signal is of primordial origin [15, 17–21]. The first detection of an SGWB gives hope that future GW observations will allow us to probe high-energy processes taking place in the early Universe.

Among the many candidates of primordial GW sources [22, 23], our analysis focuses on first-order phase transitions (PTs) in the early Universe. These are expected when a new minimum emerges in the effective potential of the theory as the Universe cools and thermal corrections to the potential diminish. If the PT is of first order, the new vacuum and the initial one are separated by a barrier that the scalar field will eventually cross through bubble nucleation. After nucleation, the bubbles grow due to the latent heat released from the difference between the true and the false vacua and eventually collide, filling the whole volume with the new phase. An SGWB is expected to be sourced by the anisotropic stresses due to the collisions of bubbles and highly relativistic fluid shells in very strong transitions [24–32], as well as the subsequent development of bulk fluid motion [33–35]. The latter initially takes the form of sound waves [36–42], but can also lead to the development of magnetohydrodynamic (MHD) turbulence [43–55]. Depending on the underlying PT model and the consequent bubble and plasma dynamics, any of these GW sourcing mechanisms may dominate the SGWB production, and we therefore include all of them in our analysis. Turbulence has often been neglected in previous analyses for two reasons: because it was considered subdominant, and because of the absence of a simulation-validated template for the GW signal [35]. However, it is now clear that the non-observation of turbulence in simulations of weakly first-order PTs does not imply that it is never formed or always subdominant, in particular, if the lifetime of the sound waves is shorter than one Hubble time [35, 56–58]. Furthermore, a simulation-validated template has been developed for the SGWB produced by fully developed turbulence [53, 55], which we will use in the following.

Our focus will be on the Laser Interferometer Space Antenna (LISA) mission [59], aimed at probing the currently unexplored GW frequency band around the milli-Hertz. In terms of cosmology, this band is associated with energies in the early Universe around

the electroweak scale [23]. Many extensions of the Standard Model (SM) predict the electroweak PT to be of first order, which is a strong motivation to look for associated GW signals in LISA [34, 35]. In this work, we pursue two main goals. First, we select a set of templates for GW sourcing processes associated with first-order PTs, in order to initiate a template repository for the pipeline of SGWB searches that we have developed. We stress that some underlying assumptions and approximations still affect these templates. While they cannot be considered as carved into stone, we are confident that they represent the best available choices combining simplicity and accuracy, given the state of the art in the field. Second, we implement these templates in the `SGWBinner` code [60, 61], and use them to produce forecasts of the sensitivity of LISA to SGWBs from first order PTs, studying in particular its impact on the reconstruction of the parameters of two examples of particle physics models underlying the transition.

With respect to previous works focused on the case of GW production by sound waves [62–65], we add parameter estimation also for the GW signals from bubble collisions and MHD turbulence. We assess the LISA sensitivity in terms of two different sets of parameters: in terms of thermodynamic parameters (cf. Sec. 5), such as the kinetic energy fraction, the temperature, and the duration of the transition, as well as in terms of geometric parameters (cf. Sec. 4), such as the frequency breaks and the amplitude of the SGWB and provide a mapping between the two sets. Compared to previous analyses [62–65], we go one step further in the process and translate the estimation of the SGWB template parameters into constraints on the parameter space of two specific particle physics models (cf. Sec. 6). Concerning the SGWB from sound waves, we adopt a somewhat simpler template than in Refs. [62–65], based on the results of Ref. [42]. The main features of the SGWB spectrum (spectral shape and position of the spectral breaks) are consistent with the results developed in Refs. [40, 62, 65]. However, the spectral slopes of the SGWB are taken from Ref. [42]. These are compatible with the recent results of Refs. [58, 66] (see also Ref. [55]). Note that the spectral shape of the SGWB sourced by sound waves in the context of the sound shell model [40, 67] is still a subject of active study [58, 66, 68].

The LISA mission has recently been adopted by the European Space Agency (ESA) and its construction will start soon for a launch scheduled in the 2030s. Our results serve as a starting point for the main task ahead of the community in preparation of the experiment, which is the development of the pipelines for the data analysis and the physics interpretation. We make some simplifying assumptions in our analyses of the forecasts. We neglect the theoretical uncertainties associated with the computation of the transition parameters and the resulting GW signal in a given model [69–72]. The impact of these uncertainties on the parameter reconstruction was recently studied in Ref. [73]. However, this is an active research topic [74–81] and we assume significant progress will be made towards reducing this issue by the time the data becomes available. Another kind of theoretical uncertainty that we neglect are general relativity effects, important especially when the average bubble size is comparable in size to the Hubble scale [82]. Their exact effect on the SGWB spectra is still uncertain. Furthermore, we adopt a simple two-parameter noise model to predict the performance of the mission. While it is simplistic to assume that one can directly apply a pre-flight validated instrument noise model in a realistic search for the SGWB in

real data, the development of methodologies to incorporate noise uncertainties in SGWB searches is a subject of ongoing study [83–85]. We plan to update our predictions as more realistic noise estimates, as well as methods of coincident noise and SGWB estimation, are produced by the LISA Consortium. We use simplified, template-based predictions for the astrophysical foregrounds. The impact of astrophysical foregrounds on the reach of LISA will very likely be significant [86–90]. Also in this aspect, we plan to improve our results in the future, when the methods for disentangling the primordial SGWB from the astrophysical foregrounds improve further. We work on simulated data including only the SGWB, the foregrounds, and the instrument noise: therefore, we assume that the data stream can be perfectly cleaned from residuals due to the imperfect subtraction of the signals of other GW sources. Moreover, the data are also simulated adopting the very same templates for the noise, foregrounds and SGWB which we adopt in the reconstruction: hence, we also implicitly assume that any theoretical and experimental uncertainties are absent, and the models reproduce faithfully the reality of the signals and the noise. Last but not least, we limit our discussion to parameter reconstruction only, and leave the question of model discrimination, taking into account also other SGWB sources not related to PTs, for future work.

This paper is organised as follows. In Sec. 2, we introduce the SGWB templates in terms of the “geometric parameters” such as the amplitude, characteristic frequencies, and spectral slopes, and specify how these depend on the “thermodynamic PT parameters” such as kinetic energy fraction in the plasma, the transition temperature and inverse timescale of the transition. Section 3 describes the `SGWBinner` code and the data analysis strategy. We then proceed with evaluating the parameter reconstruction for cosmological PTs in terms of different sets of parameters. In Sec. 4, we perform the SGWB spectrum reconstruction in terms of the geometric parameters. In Sec. 5, we address the reconstruction of the thermodynamic parameters related to the dynamics of the PT. Finally, Sec. 6 connects the PT parameters to two particular underlying particle physics models, reconstructing the “fundamental model parameters” such as masses and couplings. We conclude in Sec. 7.

2 SGWB templates for first-order phase transitions

Cosmological first-order PTs generate GWs predominantly via three mechanisms: collisions of the vacuum bubble walls, sound waves in the primordial plasma, and turbulent motion. The corresponding SGWB spectra of the former can be modeled as a broken power law (BPL), whereas the latter two can be described in terms of double broken power laws (DBPLs). The respective amplitudes and frequency breaks depend on several parameters, which under some assumptions (to be clarified later for each source) can be related to the strength of the PT α , its inverse duration normalised to the Hubble rate β/H_* , the temperature T_* after the end of the transition, and the bubble wall velocity ξ_w [91]. Furthermore, the turbulence SGWB will also depend on the fraction of energy ε converted into turbulent motion in the PT.

The present-day frequencies and amplitudes are related to the quantities at the time of GW production (with subscript “*”) via the relations

$$f = f_* \frac{a_*}{a_0} = H_{*,0} \frac{f_*}{H_*}, \quad h^2 \Omega = h^2 F_{\text{GW},0} \Omega_*, \quad (2.1)$$

where $H_{*,0}$ is the Hubble rate at the time of GW production H_* redshifted to today,

$$H_{*,0} = \frac{a_*}{a_0} H_* \simeq 1.65 \times 10^{-5} \text{ Hz} \left(\frac{g_*}{100} \right)^{\frac{1}{6}} \left(\frac{T_*}{100 \text{ GeV}} \right), \quad (2.2)$$

and $F_{\text{GW},0}$ is the red-shift factor for the fractional energy density,

$$h^2 F_{\text{GW},0} = h^2 \left(\frac{a_*}{a_0} \right)^4 \left(\frac{H_*}{H_0} \right)^2 \simeq 1.64 \times 10^{-5} \left(\frac{100}{g_*} \right)^{1/3}, \quad (2.3)$$

with $H_0 = 100 h \text{ km/s/Mpc}$. Here, g_* is the effective number of degrees of freedom at the end of the PT, which we assume to approximately be the same as the number of entropy degrees of freedom $g_* \approx g_{*s}$, as appropriate for $T_* > 0.1 \text{ MeV}$ [92]. We will now proceed to describe the SGWB templates through both sets of geometric and thermodynamic parameters corresponding to the underlying sources, and refer to them as $\vec{\theta}_{\text{Cosmo}}$ in each case.

2.1 Template I: broken power law for bubble collisions and highly relativistic fluid shells

Template I is a broken power law (BPL) that can be expressed as

$$\Omega_{\text{GW}}^{\text{BPL}}(f, \vec{\theta}_{\text{Cosmo}}) = \Omega_b \left(\frac{f}{f_b} \right)^{n_1} \left[\frac{1}{2} + \frac{1}{2} \left(\frac{f}{f_b} \right)^{a_1} \right]^{\frac{n_2 - n_1}{a_1}}, \quad (2.4)$$

where $\vec{\theta}_{\text{Cosmo}} = \{\Omega_b, f_b\}$ is the set of free geometric parameters of the template, while n_1, n_2 , and a_1 are geometric parameters fixed by the underlying modelling of the source, as described below. The amplitude is normalised such that $\Omega(f_b) = \Omega_b$. At $f \ll f_b$ the spectrum grows as f^{n_1} , and at $f \gg f_b$ it decreases (assuming $n_2 < 0$) as f^{n_2} . The parameter a_1 describes how broad is the transition around the spectral peak. Note that, in general, f_b does not coincide with the peak of the spectrum, located at $f_p = f_b (-n_1/n_2)^{1/a_1}$, and Ω_b does not correspond to the value of the spectrum at the peak (unless $n_1 = -n_2$), which is

$$\Omega_p = \Omega_b \left[\frac{1}{2} \left(-\frac{n_2}{n_1} \right)^{\frac{n_1}{n_1 - n_2}} + \frac{1}{2} \left(-\frac{n_1}{n_2} \right)^{-\frac{n_2}{n_1 - n_2}} \right]^{-\frac{n_1 - n_2}{a_1}}. \quad (2.5)$$

Then, the SGWB spectrum can alternatively be expressed in terms of the spectral peak f_p and its value at the peak Ω_p ,

$$\Omega_{\text{GW}}^{\text{BPL}}(f, \vec{\theta}_{\text{Cosmo}}) = \Omega_p \frac{(n_1 - n_2)^{\frac{n_1 - n_2}{a_1}}}{\left[-n_2 \left(\frac{f}{f_p} \right)^{-\frac{n_1 a_1}{n_1 - n_2}} + n_1 \left(\frac{f}{f_p} \right)^{-\frac{n_2 a_1}{n_1 - n_2}} \right]^{\frac{n_1 - n_2}{a_1}}}. \quad (2.6)$$

While the functional form Eq. (2.6) is more commonly used in the literature [26, 31, 32, 93], in the following we will work with Eq. (2.4), which directly resembles the DBPL given in Eq. (2.8).

We use the BPL template, Eq. (2.4), for GW production in very strong PTs. These transitions are defined by the vacuum energy of the scalar field dominating over the radiation background, i.e. $\alpha \gg 1$. One possibility for the time evolution of the bubbles is that the walls interact sufficiently weakly with the surrounding plasma and thus most of the released vacuum energy goes to the bubble wall gradient and kinetic energies [94]. In such a transition, plasma motion can be neglected and the dominant source of GWs comes from the scalar field. The production of GWs in such a system was modelled with the envelope approximation [25, 95], in which the collided parts of the bubble walls are neglected in the thin wall limit, and further developed in e.g. Refs. [26, 96, 97].

However, the collided part of the bubble walls has recently been found to be essential for a correct estimation of the SGWB spectrum, since in reality, the shells cannot lose their momentum instantaneously. Such a possibility has been pointed out in numerical simulations [27, 28, 98, 99] and from analogies with particle collisions [100]. While for maximally long-lived shells a modeling called bulk flow was proposed and has been studied numerically and analytically [93, 100], it is not obvious how the collided part decays in specific particle physics models. In this regard, we adopt a hybrid approach developed in Refs. [29, 31] for the time evolution of the collided walls and the resulting GW production. In these studies, time evolution of the momentum decay in the radial direction is embedded in multi-bubble nucleation and collision histories, allowing for the calculation of the SGWB spectrum in microphysics potentials that can realistically cause strongly supercooled PTs.

While the dominant energy carrier in the weak coupling limit is the scalar field, supercooled PTs can also proceed with relativistic detonations, in which the vacuum energy is dominantly transferred to highly relativistic fluid shells. In this energy transfer, particle splitting plays a key role [101–105]. As a result, the wall reaches a terminal velocity and the main energy carriers are the highly relativistic fluid shells surrounding the bubbles. The production of GWs for this case is expected to be qualitatively different from that of sound waves because, in the former case, the fluid shells become very thin and highly concentrated around the walls, and thus the macroscopic distribution of the energy-momentum tensor is expected to be rather similar to that of scalar walls [32, 33, 106]. In Ref. [32], the SGWB spectrum has been estimated by incorporating the radial time evolution of highly relativistic fluid shells. It was shown that the resulting SGWB spectrum is closer to the one found in the case of bubble wall collisions in models featuring the breaking of a gauge symmetry discussed in Ref. [31], which allows us to use the same SGWB template in both cases.

In this context, the peak amplitude and frequency at the present time are related to the parameters α , β/H_* , and T_* via

$$h^2\Omega_p = h^2 F_{\text{GW},0} A_{\text{str}} \tilde{K}^2 \left(\frac{H_*}{\beta} \right)^2, \quad f_p \simeq 0.11 H_{*,0} \frac{\beta}{H_*}, \quad (2.7)$$

GW source	power law template	n_1	n_2	n_3	a_1	a_2
strong PT, Sec. 2.1	BPL, Eq. (2.4)	2.4	-2.4	—	1.2	—
sound waves, Sec. 2.2.1	DBPL, Eq. (2.8)	3	1	-3	2	4
turbulence, Sec. 2.2.2	DBPL, Eq. (2.8)	3	1	-8/3	4	2.15

Table 1: Spectral slopes of the BPL and DBPL templates used for the respective GW sources from PTs.

where $\tilde{K} \equiv \alpha/(1 + \alpha)$ is the fractional energy density of the GW source. The spectrum was computed assuming a very strong transition with $\alpha \gg 1$, corresponding to $\tilde{K} \approx 1$. However, we leave \tilde{K} as a free parameter in the reconstruction (cf. Sec. 5) to take into account non-standard scenarios such as a PT taking part in a dark sector whose energy density is only a fraction of the total [107, 108]. We will focus on the most generic case of either gauged scalar field bubble collisions or highly relativistic fluid shells sourcing the SGWB. In this case, the numerical simulations of Ref. [32] indicate $A_{\text{str}} \simeq 0.05$, and the 0.11 factor in f_p of Eq. (2.7). The corresponding parameters in Eq. (2.4) are found to be $n_1 = -n_2 \simeq 2.4$ and $a_1 \simeq 1.2$ [32]. In this case, $f_b = f_p$ and $\Omega_b = \Omega_p$. Note that at scales larger than the horizon scale at the time of the transition, the SGWB spectrum would be expected to scale as f^3 because the source is uncorrelated [109]. We do not directly include this effect because the spectra we use were computed with simulations that do not take into account the expansion and the exact impact is uncertain [32]. For convenience, Tab. 1 summarizes the spectral slopes used in this work for the respective contribution to the SGWB spectrum. The geometric free parameters $\{f_b, \Omega_b\}$ can be expressed through the thermodynamic free parameters $\vec{\theta}_{\text{Cosmo}} = \{\tilde{K}, \beta/H_*, T_*\}$ via Eq. (2.7). The dependence of the spectrum on \tilde{K} , β/H_* , and T_* is illustrated in Fig. 1a.

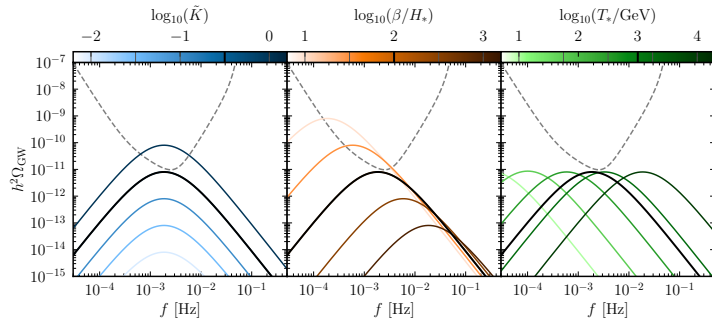
2.2 Template II: double broken power law

Template II is a double broken power law (DBPL) which takes the form

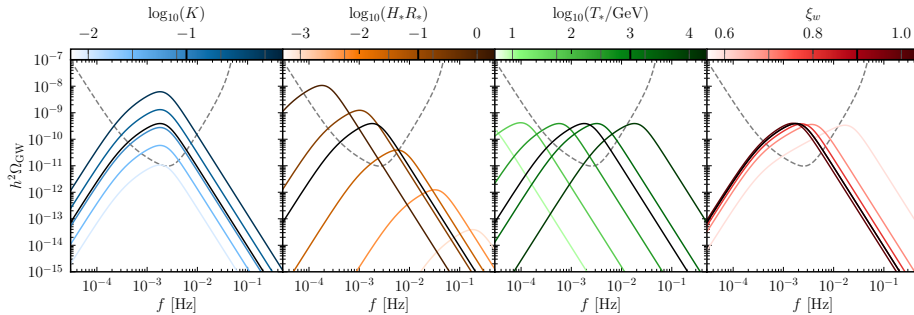
$$\Omega_{\text{GW}}^{\text{DBPL}}(f, \vec{\theta}_{\text{Cosmo}}) = \Omega_{\text{int}} \times S(f) = \Omega_2 \times S_2(f), \quad (2.8)$$

$$S(f) = N \left(\frac{f}{f_1} \right)^{n_1} \left[1 + \left(\frac{f}{f_1} \right)^{a_1} \right]^{-\frac{n_1+n_2}{a_1}} \left[1 + \left(\frac{f}{f_2} \right)^{a_2} \right]^{-\frac{n_2+n_3}{a_2}},$$

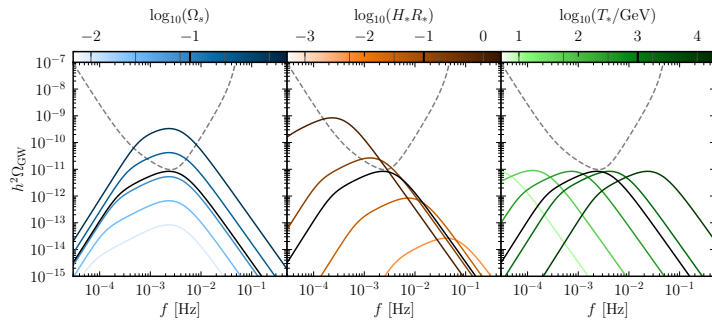
where the SGWB spectrum is decomposed into the amplitude Ω_{int} , corresponding to the value of the spectrum logarithmically integrated over the frequency, and the shape function $S(f)$. The spectrum behaves as $\Omega_{\text{GW}}^{\text{DBPL}} \propto f^{n_1}$ ($f < f_1$), f^{n_2} ($f_1 < f < f_2$), and f^{n_3} ($f_2 < f$) from low to high frequencies. The parameters a_1 and a_2 describe how smoothly the power law behavior changes at $f \sim f_1$ and $f \sim f_2$, respectively. In principle, the normalization factor N is determined from $\int_{-\infty}^{\infty} d \ln f S(f) = 1$. However, as we cannot write an analytical expression for N for arbitrary slopes and frequency breaks, we normalise the spectrum so that $S_2(f_2) = 1$, i.e. $S_2(f) = S(f)/S(f_2)$, and use the amplitude Ω_2 at the second frequency break instead of the integrated amplitude Ω_{int} . Thus, $\vec{\theta}_{\text{Cosmo}} = \{\Omega_2, f_1, f_2\}$ is the set of



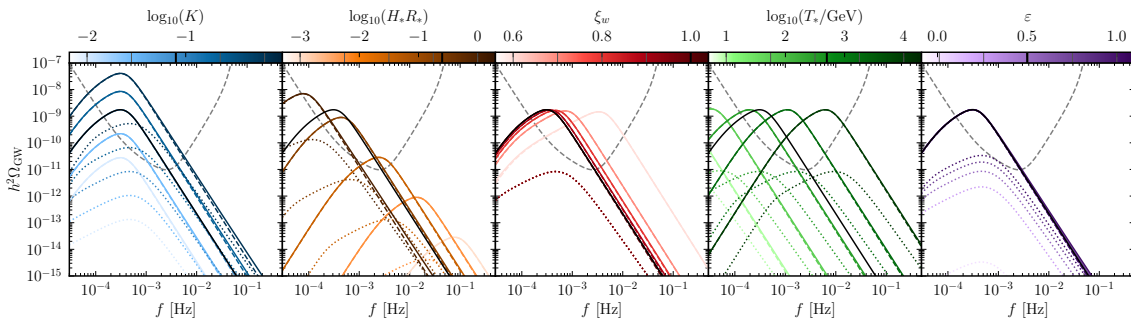
(a) bubble collisions and highly relativistic fluid shells (black: $\tilde{K} = 0.32$, $\beta/H_* = 100$, $T_* = 1$ TeV)



(b) sound waves (black: $K = 0.1$, $H_* R_* = 0.1$, $\xi_w = 0.9$, $T_* = 1$ TeV)



(c) turbulence (black: $\Omega_s = 0.1$, $H_* R_* = 0.1$, $T_* = 1$ TeV)



(d) sound waves + turbulence (black: $K = 0.08$, $H_* R_* = 0.25$, $\xi_w = 1$, $T_* = 500$ GeV, $\varepsilon = 0.5$)

Figure 1: The coloured lines show the parameter dependence of the SGWB templates for PTs in terms of the thermodynamic parameters, varying one parameter at a time. The remaining parameters are fixed to the benchmark values indicated in the subcaptions, corresponding to the black spectrum in each plot. From top to bottom we show bubble collisions, sound waves, turbulence, and sound waves + turbulence. For the latter, the spectra of the sound waves and turbulence contributions are shown as dashed and dotted lines, respectively. The dashed gray line is the LISA noise curve.

free geometric parameters of this template, while n_1 , n_2 , n_3 , a_1 , and a_2 are parameters fixed by the underlying modelling of the source.

2.2.1 Sound waves

If the coupling between the bubble walls and plasma particles is large enough, the latent heat is transferred also to the bulk motion of the fluid. While the fluid motion in general has both compression and shear components, the former dominates the latter at the initial stage of the transition because of the initial condition set by expanding spherical bubbles. After bubbles collide, compression waves propagate acting as a source of GWs. This behavior is found in numerical simulations [36–39], and the sound shell model [40, 67] is proposed to explain it. The results show that both the sound shell thickness and the bubble size at the collision time are imprinted on the SGWB spectrum. At later times, vortical motion of the fluid can be produced by, for example, the non-linearities of the fluid or the presence of primordial magnetic fields. In this case, MHD turbulence would develop in the primordial plasma. This additional source of GWs is presented in the next subsection.

The aforementioned simulations solve the system of the fluid variables and the scalar field on a lattice, coupling both sectors via a phenomenological friction parameter. On the other hand, taking into account the large hierarchy between the scale of bubbles of cosmological size (with a sizable fraction of the Hubble radius) and that of the Higgs field, which varies within the bubble thickness (of the electroweak scale or higher), the effects of the Higgs field can be considered local to the bubble. Therefore, one can integrate out the dynamics of the Higgs field and treat the expansion of the true vacuum as a space- and time-dependent background, thus removing numerical difficulties associated with resolving the scalar field in the fluid dynamics, which can then be solved separately. Such a “Higgsless” approach has been pursued in Refs. [41, 42]. In these studies, shock waves in the plasma are also resolved with an appropriate numerical scheme [110] and are accurately incorporated into the simulation.

The SGWB spectrum from sound waves is well described by the DBPL of Eq. (2.8) that encodes the typical fluid shell thickness and the bubble size. In particular, the frequency breaks are found to be [42, 111]

$$f_1 \simeq 0.2 H_{*,0} (H_* R_*)^{-1}, \quad f_2 \simeq 0.5 H_{*,0} \Delta_w^{-1} (H_* R_*)^{-1}, \quad (2.9)$$

where $\Delta_w = \xi_{\text{shell}} / \max(\xi_w, c_s)$, with ξ_{shell} being the dimensionless sound shell thickness and c_s the speed of sound. $H_{*,0}$ is given in Eq. (2.2). For the integrated amplitude Ω_{int} , the parametric dependence is [42, 111]

$$h^2 \Omega_{\text{int}} = h^2 F_{\text{GW},0} A_{\text{sw}} K^2 (H_* \tau_{\text{sw}}) (H_* R_*), \quad (2.10)$$

where $F_{\text{GW},0}$ is given in Eq. (2.3). Here, τ_{sw} is the duration of the sound wave source and R_* the average bubbles size, estimated as [35]

$$H_* R_* = (8\pi)^{1/3} \max(\xi_w, c_s) \frac{H_*}{\beta}. \quad (2.11)$$

The constant $A_{\text{sw}} \simeq 0.11$ in Eq. (2.10) is computed from the average over the simulation data points with different values of α and ξ_w [42, 111]. The kinetic energy fraction is $K \simeq 0.6 \kappa \alpha / (1 + \alpha)$, where κ denotes the kinetic energy fraction of a single expanding bubble, derived in Ref. [91] for a perfect fluid with an ultra-relativistic equation of state, i.e. with speed of sound $c_s^2 = 1/3$ (see Refs. [112, 113] for a generalization). The factor 0.6 accounts for the efficiency in producing kinetic energy in the bulk fluid motion with respect to the single bubble case, as found in Ref. [42] (see discussion in Ref. [111]). It constitutes a conservative estimate with respect to what was assumed, e.g. in Ref. [35].

The dependence of the other parameters entering the sound waves SGWB spectrum in Eqs. (2.9) and (2.10) is as follows. The dimensionless shell thickness is calculated from the profile of an expanding bubble as $\xi_{\text{shell}} = \xi_{\text{front}} - \xi_{\text{rear}} = |\xi_w - c_s|$, where the last equality holds for subsonic deflagrations and detonations, the latter being the cases we focus on in this work, as we set ξ_w close to unity. The relative duration of the GW source, $H_* \tau_{\text{sw}} = \min[H_* \tau_{\text{sh}}, 1]$, corresponds either to the estimated decay time into turbulence, $H_* \tau_{\text{sh}} = H_* R_* / \sqrt{\bar{v}_f^2}$, if the latter is shorter than the Hubble time [35]; or to the Hubble time itself. The first case is expected for relatively strong transitions corresponding to large bulk fluid velocities [57]. Note that we will nevertheless adopt the average fluid velocity expression $\bar{v}_f^2 = \Gamma^{-1} K$ valid in the subrelativistic bulk velocity limit, where $\Gamma = \bar{w}/\bar{e}$ is the mean adiabatic index, which is $\Gamma = 4/3$ for a radiation fluid [35]. In the second case, i.e. when the sound source duration is comparable to the Hubble time, the scaling of the SGWB spectral amplitude becomes $\Omega_{\text{int}} \propto (H_* R_*) \propto (H_*/\beta)$, in contrast to $\Omega_p \propto (H_*/\beta)^2$ for bubble collisions, indicating that the sourcing lasts longer for sound waves.

For the exponents we use the result of Ref. [42] and take $n_1 = 3$, $n_2 = 1$, $n_3 = -3$, $a_1 = 2$, and $a_2 = 4$, cf. Tab. 1. The amplitude at f_2 is then related to the integrated amplitude, Eq. (2.10), via

$$\Omega_2 = \frac{1}{\pi} \left(\sqrt{2} + \frac{2 f_2/f_1}{1 + f_2^2/f_1^2} \right) \Omega_{\text{int}} \approx 0.55 \Omega_{\text{int}}, \quad (2.12)$$

where the approximate sign holds for $\xi_w \approx 1$. The SGWB spectrum is then completely fixed once the thermodynamic free parameters $\vec{\theta}_{\text{Cosmo}} = \{K, H_* R_*, \xi_w, T_*\}$ are set. The dependence of the SGWB spectrum on the input parameters K , $H_* R_*$, ξ_w , and T_* is illustrated in Fig. 1b.

2.2.2 Magnetohydrodynamic turbulence

The source of GWs from MHD turbulence is a combination of the anisotropic stresses produced by velocity and magnetic fields. Following Ref. [35], we insert an unknown parameter ε to represent the fraction of overall kinetic energy in bulk motion that is converted to MHD turbulence. We define the parameter

$$\Omega_s = \Omega_{\text{kin}} + \Omega_{\text{mag}} = \varepsilon K, \quad (2.13)$$

representing the total energy density fraction in the GW source from turbulence, where Ω_{mag} and Ω_{kin} are the corresponding magnetic (mag) and kinetic (kin) energy density

fractions. Furthermore, we assume that the turbulence is fully developed at the beginning of the sourcing process and that equipartition between the turbulent kinetic and magnetic energies is reached [114], $\Omega_{\text{mag}} \approx \Omega_{\text{kin}}$, so that

$$\bar{v}_f^2 \approx \bar{v}_A^2 \approx \Gamma^{-1} \varepsilon K = \frac{3}{4} \Omega_s, \quad (2.14)$$

where \bar{v}_f is the characteristic fluid velocity and \bar{v}_A is the Alfvén speed, both approximated in the subrelativistic limit. The turbulence SGWB spectral peak is located at the energy injection scale, which we assume to be the bubbles separation at the end of the PT, R_* [47]. The characteristic length scale of the MHD turbulence relative to the Hubble scale at the moment of the GW sourcing determines the frequency at which the SGWB spectrum peaks, $f_p \simeq 1.4 H_{*,0} (H_* R_*)^{-1}$ [53, 55], where $H_{*,0}$ and $H_* R_*$ are given by Eqs. (2.2) and (2.11), respectively. Another important parameter in the model is the duration of the GW source, which can be inferred from MHD simulations and is of the order of a few eddy turnover times, $\mathcal{N} \tau_e = \mathcal{N} R_* / [2\pi \max(\bar{v}_f, \bar{v}_A)] \simeq \mathcal{N} R_* / (2\pi \bar{v}_A)$, with $\mathcal{N} \simeq 2$ [53, 55] (note that the definition of τ_e differs from the one in Ref. [55] by a factor $1/2\pi$).

The SGWB from MHD turbulence can be written as [53, 55]

$$\Omega_{\text{GW}}^{\text{MHD}}(f, \vec{\theta}_{\text{Cosmo}}) = 3 \mathcal{A} \Omega_s^2 F_{\text{GW}} (H_* R_*)^3 (f/H_{*,0})^3 p_{\bar{\Pi}}(f, H_* R_*) \mathcal{T}(f, \mathcal{N} H_* \tau_e), \quad (2.15)$$

where the amplitude is¹ $\mathcal{A} \simeq 0.085$, the spectrum of the anisotropic stresses can be approximated as [55]

$$p_{\bar{\Pi}}(f, H_* R_*) = \left[1 + \left(\frac{f}{f_2} \right)^{a_2} \right]^{-\frac{11}{3a_2}}, \quad \text{with } f_2 \simeq 2.2 \frac{H_{*,0}}{H_* R_*} \quad \text{and } a_2 \simeq 2.15, \quad (2.16)$$

and the function \mathcal{T} is [53, 55]

$$\mathcal{T}(f, \mathcal{N} H_* \tau_e) = \begin{cases} \ln^2 [1 + \mathcal{N} H_* \tau_e], & \text{if } 2\pi f / H_{*,0} \leq (\mathcal{N} H_* \tau_e)^{-1}, \\ \ln^2 [1 + H_{*,0} / (2\pi f)], & \text{if } 2\pi f / H_{*,0} > (\mathcal{N} H_* \tau_e)^{-1}. \end{cases} \quad (2.17)$$

The function \mathcal{T} can be approximated to a BPL as

$$\mathcal{T}(f, \mathcal{N} H_* \tau_e) = \left(\frac{H_{*,0}}{2\pi f_1} \right)^2 \left[1 + \left(\frac{f}{f_1} \right)^{a_1} \right]^{-\frac{2}{a_1}}, \quad (2.18)$$

where the position of the break f_1 and the smoothness parameter a_1 , shown in Fig. 2, depend on the eddy turnover time,

$$f_1(\mathcal{N} \tau_e) = \frac{H_{*,0}}{2\pi} \ln^{-1}(1 + \mathcal{N} H_* \tau_e) \approx \frac{H_{*,0}}{2\pi \mathcal{N} H_* \tau_e} = \frac{\bar{v}_A}{\mathcal{N}} \frac{H_{*,0}}{H_* R_*}. \quad (2.19)$$

In the above equation, we have assumed that $\mathcal{N} H_* \tau_e = \mathcal{N} H_* R_* / (2\pi \bar{v}_A) \ll 1$: this holds in general whenever the MHD turbulence SGWB is large enough to be observable, i.e. in the regime where $\bar{v}_A \sim \sqrt{\Omega_s}$ is large, meaning that the PT is strongly first order (large α). In this limit, the parameter a_1 can be approximated as a constant, $a_1 = 4$, for $\mathcal{N} H_* \tau_e \lesssim 0.3$ (or, equivalently, for $H_* R_* \lesssim \bar{v}_A$ since $\mathcal{N} \simeq 2$).

¹For simplicity and to take into account the average of the SGWB spectrum over oscillations in time, the parameter \mathcal{A} here corresponds to $\mathcal{C}/(2\mathcal{A}^2)$ in Ref. [53], similar to Ref. [55].

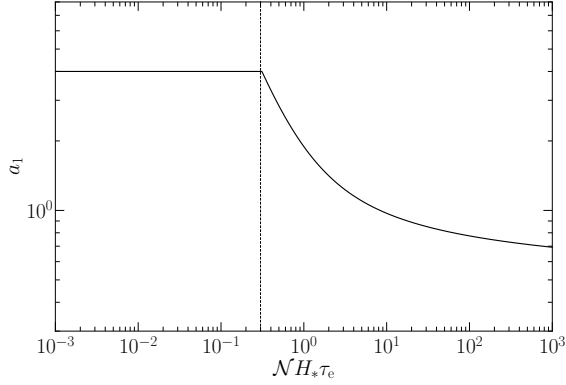


Figure 2: Smoothness parameter a_1 of the MHD turbulence SGWB as a function of the normalised eddy turnover time. It is set to 4 for values below the dashed vertical line corresponding to $\mathcal{N}H_*\tau_e = 0.3$ as larger values of a_1 do not significantly influence the DBPL template.

The resulting MHD turbulence SGWB can be expressed in terms of the DBPL model of Eq. (2.8) setting $n_1 = 3$, $n_2 = 1$, $n_3 = -8/3$, $a_1 = 4$, and $a_2 \simeq 2.15$,

$$\Omega_{\text{GW}}^{\text{MHD}}(f, \vec{\theta}_{\text{Cosmo}}) = \frac{3\mathcal{A}\bar{v}_A\Omega_s^2(H_*R_*)^2}{4\pi^2\mathcal{N}} F_{\text{GW},0} \times \left(\frac{f}{f_1}\right)^3 \left[1 + \left(\frac{f}{f_1}\right)^{a_1}\right]^{-\frac{2}{a_1}} \left[1 + \left(\frac{f}{f_2}\right)^{a_2}\right]^{-\frac{11}{3a_2}}. \quad (2.20)$$

Note that expressed in this form, the amplitude of the SGWB seems to be proportional to $\bar{v}_A\Omega_s^2 \sim \Omega_s^{\frac{5}{2}}$. This is actually not the case, because f_1 is a function of \bar{v}_A . We find from Eqs. (2.16) and (2.19) that the ratio between the frequency breaks is

$$\frac{f_2}{f_1} = \frac{2.2\mathcal{N}}{\bar{v}_A} \simeq \frac{2.5\mathcal{N}}{\sqrt{\Omega_s}} \gg 1. \quad (2.21)$$

This ratio is in general large since $\bar{v}_A < 1$, so that $f_2/f_1 \gtrsim 5$ with $\mathcal{N} \simeq 2$. This property allows us to find the amplitude Ω_2 used in the DBPL template in Eq. (2.8). At frequencies $f/f_1 \gg 1$, the SGWB spectrum can be approximated by a single BPL,

$$\Omega_{\text{GW}}^{\text{MHD}}(f \gg f_1, \vec{\theta}_{\text{Cosmo}}) = \frac{3\mathcal{A}\bar{v}_A\Omega_s^2(H_*R_*)^2}{4\pi^2\mathcal{N}} F_{\text{GW},0} \left(\frac{f}{f_1}\right) \left[1 + \left(\frac{f}{f_2}\right)^{a_2}\right]^{-\frac{11}{3a_2}}, \quad (2.22)$$

from which one can derive

$$h^2\Omega_2 = h^2 F_{\text{GW},0} A_{\text{MHD}} \Omega_s^2 (H_*R_*)^2, \quad (2.23)$$

with $A_{\text{MHD}} = 3 \times 2.2\mathcal{A}/(4\pi^2) \times 2^{-11/(3a_2)} \simeq 4.37 \times 10^{-3}$. Here the correct physical scaling $\Omega_2 \sim \Omega_s^2$ is recovered. Finally, using the value of Ω_2 in Eq. (2.23) and the expression for the SGWB in Eq. (2.20), we can reproduce the DBPL template in Eq. (2.8) with

$$S_2(f) = 2^{\frac{11}{3a_2}} \left(\frac{f_1}{f_2}\right) \left(\frac{f}{f_1}\right)^3 \left[1 + \left(\frac{f}{f_1}\right)^{a_1}\right]^{-\frac{2}{a_1}} \left[1 + \left(\frac{f}{f_2}\right)^{a_2}\right]^{-\frac{11}{3a_2}}. \quad (2.24)$$

The peak of the SGWB spectrum in the template of Eq. (2.8) is not located exactly at f_2 . Under the assumption $f_p/f_1 \sim f_2/f_1 \gg 1$, we can find the position of the spectral peak $f_p = f_2(-n_2/n_3)^{1/a_2} \simeq 0.6f_2 \simeq 1.4H_{*,0}(H_*R_*)^{-1}$ [53, 55], and the SGWB amplitude at the peak using Eq. (2.5), $\Omega_p \simeq 1.2\Omega_2$.

To wrap up, the parameters that characterise the SGWB spectrum from MHD turbulence are Ω_s , H_*R_* , and T_* , from which we can derive the free geometric parameters of the DBPL,

$$f_1 = \frac{\sqrt{3}\Omega_s}{2\mathcal{N}} H_{*,0}(H_*R_*)^{-1}, \quad f_2 \simeq 2.2H_{*,0}(H_*R_*)^{-1}, \quad (2.25)$$

$$h^2\Omega_2 = h^2F_{\text{GW},0} A_{\text{MHD}} \Omega_s^2 (H_*R_*)^2,$$

with the exponents of the DBPL summarised in Tab. 1. Note that Ω_s and H_*R_* can be related to the PT parameters using Eqs. (2.11) and (2.13), and the relation $K \simeq 0.6\kappa\alpha/(1+\alpha)$ given in Sec. 2.2.1.

The parameter dependence on Ω_s , R_*H_* , and T_* of the spectrum is depicted in Fig. 1c. In realistic scenarios of first-order PTs, the full SGWB spectrum consists of the sum of both contributions due to the fluid motion, sound waves and turbulence, in which case it can be parameterised in terms of $\vec{\theta}_{\text{Cosmo}} = \{K, R_*H_*, \xi_w, T_*, \varepsilon\}$, as illustrated in Fig. 1d.

3 Parameter reach and reconstruction

The `SGWBinner` code has been originally designed to carry out agnostic searches and reconstructions of the primordial SGWB signal at LISA [60, 61], and used to quantify the instrument capabilities [115, 116]. In such agnostic searches, the code reconstructs the primordial signal as power laws in multiple bins of optimal widths, while using templates only for the astrophysical foregrounds. The agnostic search is flexible but sub-optimal when a precise template of the primordial signal is available. For this work (and the companion papers [117, 118]), we have developed a new functionality of the `SGWBinner`: a template-based analysis of the primordial signal. We present it below, starting with a review of the foundations of the LISA measurement. We also initiate a template bank within the code, including all the signals discussed in the previous section, preparing the tools to facilitate SGWB searches of cosmological first-order PTs in LISA.

3.1 LISA measurement channels

LISA consists of three satellites, $i = 1, 2, 3$, with relative distances L_{ij} . At every time t , the satellite i emits and receives a laser beam to and from the satellite $j \neq i$, and measures their phases. Due to the laser frequency instabilities, the direct comparison of the phase measurements is too noisy to perform interferometry sensitive to the expected GW signals. However, this noise contribution is largely suppressed by post-processing the data and performing time delay interferometry (TDI) [119], i.e. a comparison of the phase measurements at opportune different times. Different TDI approaches exist [120–128]. Here we consider the “first generation” one, which works under the assumption that the LISA satellites are in an equilateral configuration (i.e. $L_{ij} = L$ for any i, j) and have identical

noise levels.² In the equilateral approximation, the laser phase emitted from the satellite j at time $t - L/c$ is recorded at time t in satellite i , with c being the light speed. We denote the phases $\eta_{ij}(t)$. Three measurements (suppressing the frequency instabilities) can be recast from these phases [121],

$$\mathbf{A} = \frac{\mathbf{Z} - \mathbf{X}}{\sqrt{2}}, \quad \mathbf{E} = \frac{\mathbf{X} - 2\mathbf{Y} + \mathbf{Z}}{\sqrt{6}}, \quad \mathbf{T} = \frac{\mathbf{X} + \mathbf{Y} + \mathbf{Z}}{\sqrt{3}}, \quad (3.1)$$

where

$$\mathbf{X} = (1 - D_{13}D_{31})(\eta_{12} + D_{12}\eta_{21}) + (D_{12}D_{21} - 1)(\eta_{13} + D_{13}\eta_{31}), \quad (3.2)$$

and the \mathbf{Y} and \mathbf{Z} variables are obtained through cyclic permutations of the indices. Here, $D_{ij}\eta_{kl}(t) = \eta_{kl}(t - L_{ij}/c)$ is the one-arm length delay operator. Remarkably, in the above approximations, the channels \mathbf{A} , \mathbf{E} , and \mathbf{T} constitute three virtual, orthogonal GW interferometers, with the former two being identical and the latter being a (quasi-)null channel, i.e. a channel whose sensitivity to the signal is largely suppressed. The `SGWBinner` simulates and analyses the data in these three channels, and leverages the \mathbf{T} channel property to reconstruct the satellite noise sources.

3.2 Data in each channel

The data collected via the \mathbf{A} , \mathbf{E} , and \mathbf{T} channels will contain all the transient and non-transient signals. This includes individually resolvable GW emitting events and a stochastic component, given by the sum of all unresolved astrophysical sources, of the stochastic instrumental noise components, and of possible SGWB signals. The `SGWBinner` simulates data streams of the stochastic component and forecasts posteriors for the parameters of its aforementioned contributions, under the simplifying assumption that their correlations with the transient signals and transient noises are negligible. Thus, for our purpose, the data \tilde{d}_i in the channel $i = \mathbf{A}, \mathbf{E}, \mathbf{T}$ reduce to

$$\tilde{d}_i(t) = \sum_{\nu} \tilde{n}_i^{\nu}(t) + \sum_{\sigma} \tilde{s}_i^{\sigma}(t), \quad (3.3)$$

where the first sum includes the stochastic noise components, \tilde{n}_i^{ν} , and the second sum runs over the signal contributions, \tilde{s}_i^{σ} . As we will clarify in Sec. 3.3, the noise components can be summarised in two contributions (from the test masses and the optical measurement systems), while we will focus on three signal contributions (two foregrounds and one primordial SGWB).

For simplicity, we assume all dominant noise sources to be practically stationary and Gaussian, with zero mean. Moreover, we expect the noise produced by a source common to different channels to create negligible correlations after TDI operations. In this way, the

²The robustness of the results obtained in this simplified approach against the relaxation of both these assumptions has been investigated in Ref. [129]. Such work demonstrated that, for a power law signal, a non-equilateral LISA configuration and the inclusion of up to twelve noise parameters (one per each TM/laser noise component) do not affect the reconstruction of the signal parameters significantly. Further studies considering different signal templates, e.g. the ones considered in the present work, are required to generalise this statement.

components \tilde{n}_i^ν effectively are independent, random, and Gaussian variables. In particular, \tilde{n}_A^ν and \tilde{n}_E^ν just differ by their statistical realization, while $\tilde{n}_A^\nu(t)$ (or $\tilde{n}_E^\nu(t)$) also differs from $\tilde{n}_T^\nu(t)$ due to their response function. Indeed, for identical satellites in an equilateral configuration, every satellite has statistically equivalent noise sources; furthermore, A and E have the same response functions, but A (or E) and T do not.

We also treat $\tilde{s}_i^\sigma(t)$ as independent, (zero-mean) Gaussian, and stationary variables. While this choice simplifies and speeds up the data simulation and analysis, it is suboptimal. Indeed, among our stochastic signals, the Galactic foreground is anisotropic in the cosmic microwave background (CMB) frame, yielding a non-stationary signal in the data due to the yearly rotation of the LISA satellites' plane. Averaging this non-stationary signal over several years effectively converts it to a broader Gaussian contribution that can be treated as stationary. This should not bias the whole parameter reconstruction but, at least in principle, should be less precise than an analysis including the yearly variability (cf. Sec. 3.3 for details on the averaged Galactic foreground).

Within these assumptions, we Fourier transform the data in Eq. (3.3) from time to frequency domain,

$$d_i(f) = \int_{-\tau/2}^{\tau/2} \tilde{d}_i(t) e^{-2\pi i f t} dt, \quad (3.4)$$

with statistical properties

$$\langle d_i(f) \rangle = 0, \quad \langle d_i(f) d_j^*(f') \rangle = \delta_{ij} \frac{\delta(f - f')}{2} [P_{N,ii}(f) + P_{S,ii}(f)], \quad (3.5)$$

where the brackets denote the ensemble average and τ is the time over which the Fourier transform is performed (as will be clarified in Sec. 3.4).³ Moreover, $P_{N,ii}$ and $P_{S,ii}$ are the noise and signal power spectra. They are respectively the sum of the power spectra of each noise source ν and each signal σ recorded in the i - i correlator. $P_{N,ii}$ can be expressed in terms of the i -channel response function T_{ii}^ν relative to the strain S_N^ν of the noise sources ν , reading as

$$P_{N,ii}(f) = \sum_{\nu} T_{ii}^\nu(f) S_N^\nu(f). \quad (3.6)$$

The same can be done for $P_{S,ii}$, with the peculiarity that all signal strain sources share the same response function:

$$P_{S,ii} = R_{ii}(f) \sum_{\sigma} S_S^\sigma(f) = \frac{3H_0^2}{4\pi^2 f^3} R_{ii}(f) \sum_{\sigma} h^2 \Omega_{\text{GW}}^\sigma(f), \quad (3.7)$$

with R_{ii} denoting the response function to the signals and S_S^σ the strain of the SGWBs.

For forecast studies and our level of approximations, it is reasonable to neglect the uncertainties in the response functions. For T_{ii}^ν and R_{ii} we thus adopt the response functions already implemented in the `SGWBinner` code, where all parameters have known values so

³In Eq. (3.5), the Dirac delta only arises in the limit of infinite observation time. It is however a good approximation in the frequency regime $f \ll 1/\tau$ we are interested in. The Kronecker delta instead accounts for the orthogonality of the A, E, and T channel basis emerging in the case of three identical satellites in perfectly equilateral configuration.

that there is no need to fit for them. The expressions of T_{ii}^ν and R_{ii} can be found in Appendix A.⁴

3.3 Injected (and reconstructed) noises and signals

We now describe the noise and signal source strains we implement in `SGWBinner` for the present work. Regarding the signals, we only consider the astrophysical foregrounds whose presence in the LISA data is guaranteed from other observations, namely the Galactic foreground and the one from stellar-origin black hole binaries (SOBHs). At the same time, we omit any potential cosmological SGWB besides the PT one.

Noise: LISA performs its measurements by monitoring the relative distances of the test masses (TMs) inside the satellites. The statistical errors in the GW detection are then primarily due to perturbations of the TM free fall regime, and uncertainties in the measurement of the TM relative positions. This qualitatively explains a well-investigated result: the dominant noise strains S_N^ν are given by the TM and the optical measurement system (OMS) strains [59, 131]

$$S_{ii}^{\text{TM}}(f) = A^2 \left(1 + \left(\frac{0.4 \text{ mHz}}{f} \right)^2 \right) \left(1 + \left(\frac{f}{8 \text{ mHz}} \right)^4 \right) \left(\frac{1}{2\pi f c} \right)^2 \left(\frac{\text{fm}^2}{\text{s}^3} \right), \quad (3.8)$$

$$S_{ii}^{\text{OMS}}(f) = P^2 \left(1 + \left(\frac{2 \times 10^{-3} \text{ mHz}}{f} \right)^4 \right) \left(\frac{2\pi f}{c} \right)^2 \left(\frac{\text{pm}^2}{\text{Hz}} \right), \quad (3.9)$$

where S_{ii}^{TM} models the noise relative to the non-free fall effects, and S_{ii}^{OMS} models the noise due to mismeasuring the TM distances.⁵

In our simulation, we inject the noise with the nominal values $A = 3$ and $P = 15$. In the parameter estimation of the noise and signals we adopt Gaussian priors centered on these nominal values and with 20% width [59].

Extra-Galactic foreground: It results from the superposition of the SOBHs and neutron-star binaries (NSBs) that are outside the Milky Way and that LISA does not individually resolve. LISA is sensitive to these sources when they are in the inspiral phase. Because of the statistical properties of the SOHB and NSB populations as well as the LISA angular resolution, the extra-Galactic foreground in LISA can be approximated as an isotropic signal with a power law frequency shape [132–136]

$$h^2 \Omega_{\text{GW}}^{\text{Ext}}(f) = h^2 \Omega_{\text{Ext}} \left(\frac{f}{1 \text{ mHz}} \right)^{2/3}. \quad (3.10)$$

The fiducial value and prior for Ω_{Ext} can be obtained from the population inference analyses at terrestrial interferometers [137]. By approximating one of the recent estimates [135], we use $\log_{10}(h^2 \Omega_{\text{Ext}}) = -12.38$ for the injections and a Gaussian prior around it, with $\sigma = 0.17$, for the parameter estimation.

⁴For studies on the response functions and their uncertainties see, e.g. Refs. [61, 128, 130].

⁵Such an effective description must be accompanied by opportune manipulation of the response functions; see Appendix A

Galactic foreground: The Compact Galactic Binary (CGB) population produces a loud signal in LISA coming from the Galactic disk [138]. After removing the CGBs that LISA can individually resolve, there remains a strong stochastic component which, in the LISA satellite’s frame, originates from a sky patch that moves with time and has a cycle of one year (i.e. the yearly periodicity of the LISA orbit around the Sun). Thus, due to the angular dependence of the response functions, the unresolved CGB signal integrated over the whole sky dome exhibits a strength with a yearly modulation [88, 138]. To forecast the sensitivity to cosmological PTs, one would ideally leverage the yearly modulation to better separate the astrophysical signal from the cosmological one, as done, e.g. in Refs. [64, 88]. This however requires data analysis techniques which are not yet implemented in the `SGWBinner`. In the following, we therefore only consider the whole sky-dome signal integrated over the total observing time of the mission, T_{obs} . This assumption is a conservative one. For such a signal we adopt the following template [139]:

$$h^2\Omega_{\text{GW}}^{\text{Gal}}(f) = \frac{f^3}{2} \left(\frac{f}{1 \text{ Hz}} \right)^{-\frac{7}{3}} \left[1 + \tanh \left(\frac{f_{\text{knee}} - f}{f_2} \right) \right] e^{-(f/f_1)^v} h^2\Omega_{\text{Gal}}, \quad (3.11)$$

where

$$\begin{aligned} \log_{10}(f_1/\text{Hz}) &= a_1 \log_{10}(T_{\text{obs}}/\text{year}) + b_1, \\ \log_{10}(f_{\text{knee}}/\text{Hz}) &= a_k \log_{10}(T_{\text{obs}}/\text{year}) + b_k. \end{aligned} \quad (3.12)$$

For the injection, we use the fiducial values $a_1 = -0.15$, $b_1 = -2.72$, $a_k = -0.37$, $b_k = -2.49$, $v = 1.56$, $f_2 = 6.7 \times 10^{-4} \text{ Hz}$ and $\log_{10}(h^2\Omega_{\text{Gal}}) = -7.84$ [139]. We assume all of them but $h^2\Omega_{\text{Gal}}$ to be known in the parameter estimation and adopt a Gaussian prior on $\log_{10}(h^2\Omega_{\text{Gal}})$ centered at -7.84 with width $\sigma = 0.21$.

PT SGWB: We implement Template I (i.e. the BPL representing the SGWB from bubble collisions and highly relativistic fluid shells) and Template II (i.e. the DBPL representing the SGWB from sound waves and MHD turbulence), given respectively in Secs. 2.1 and 2.2. We implement the templates both in terms of the geometric parameters that characterise the spectral templates and of the thermodynamic parameters that describe the PT and the subsequent fluid motion. The injection values and priors of the geometric and thermodynamic parameters are described in Secs. 4 and 5, respectively.

3.4 Data generation and analysis

LISA is planned to operate for at least 4.5 years up to a maximum of 10 years. However, due to antenna repointing and similar operations, some periodic data gaps are scheduled, yielding a duty cycle of about 82% [116]. This would for instance correspond to interrupting the data acquisition for two days every two weeks. We consider an intermediate scenario and set the `SGWBinner` code to work with $N_d = 126$ data segments of duration $\tau = 11.4$ days each (see Eq. (3.4)), summing up to $T_{\text{obs}} = 4$ effective years of data.

Furthermore, the `SGWBinner` works in frequency domain. We denote as $d_i^s(f_k)$ the Fourier-transformed datum of the segment $s = 1, \dots, N_d$ in the bin of frequency f_k and spacing $\Delta f = 1/\tau \simeq 10^{-6}$ Hz. To simulate the LISA data, for every signal and noise component described in Sec. 3.3, the `SGWBinner` code generates N_d Gaussian realizations at each frequency bin f_k . These bins cover the whole LISA band, which in this work we assume to be $[3 \times 10^{-5}, 0.5]$ Hz, with the required resolution Δf .

The `SGWBinner` code then performs the analysis of the mock data. In our stationary approximation, one can analyse the average value at each frequency f_k after averaging over the N_d segments. In practice, we compute “segment-averaged” data defined as $\mathcal{D}_{ii}^k \equiv \sum_{s=1}^{N_d} d_i^s(f_k) d_i^s(f_k) / N_d$. In addition, the resolution Δf is beyond the characteristic scale of the typical primordial SGWB frequency shape, making the data file heavy and slow to manipulate. For this reason, the `SGWBinner` code computes a new data set D_{ii}^k , defined on a coarser set of frequencies \bar{f}_{ii}^k statistically equivalent to the original data [60, 61]. In practice, \bar{f}_{ii}^k and D_{ii}^k are computed through inverse variance weighting, and each of the new data points is associated with a weight w_{ii}^k that accounts for the number of high-resolution points (and their variance) falling into the coarse-grained bin.

For the parameter reconstruction, the code then probes the following likelihood:

$$\ln \mathcal{L}(\vec{\theta}) = \frac{1}{3} \ln \mathcal{L}_G(\vec{\theta} | D_{ii}^k) + \frac{2}{3} \ln \mathcal{L}_{LN}(\vec{\theta} | D_{ii}^k), \quad (3.13)$$

with

$$\ln \mathcal{L}_G(\vec{\theta} | D_{ii}^k) = -\frac{N_d}{2} \sum_k \sum_i w_{ii}^k \left[1 - D_{ii}^k / D_{ii}^{\text{Th}}(\bar{f}_{ii}^k, \vec{\theta}) \right]^2, \quad (3.14)$$

$$\ln \mathcal{L}_{LN}(\vec{\theta} | D_{ii}^k) = -\frac{N_d}{2} \sum_k \sum_i w_{ii}^k \ln^2 \left[D_{ii}^{\text{Th}}(\bar{f}_{ii}^k, \vec{\theta}) / D_{ii}^k \right]. \quad (3.15)$$

Here $D_{ii}^{\text{Th}}(\bar{f}_{ii}^k, \vec{\theta})$ denotes the data predicted in our theoretical model (i.e. our overall template of the injected noises and signals), while $\vec{\theta} = \{\vec{\theta}_S, \vec{\theta}_N\}$ is the vector of the free parameters involved in the injected noises and signals’ templates, namely

$$\vec{\theta}_N = \{A, P\}, \quad \vec{\theta}_S = \{\log_{10}(h^2 \Omega_{\text{Gal}}), \log_{10}(h^2 \Omega_{\text{Ext}}), \vec{\theta}_{\text{Cosmo}}\},$$

where $\vec{\theta}_{\text{Cosmo}}$ denotes the thermodynamic or geometric parameters of the PT templates. Notice that $\ln \mathcal{L}_{LN}$ is introduced to take into account the mild non-Gaussianity that the coarse graining introduces [140–143] and the Gaussian likelihood $\ln \mathcal{L}_G$ does not properly treat. Moreover, the priors for the noises and SGWB signals should be added to Eq. (3.13) to obtain the posterior distributions, which the `SGWBinner` code determines and visualizes by calling `Polychord` [144, 145], `Cobaya` [146], and `GetDist` [147].

We finally remark that several forecast analyses use the signal-to-noise ratio (SNR) as a rule of thumb to assess whether a primordial SGWB can be detected. To help the comparison with these analyses, we will quote the SNRs of the injected PT signals. We compute it as [148]

$$\text{SNR} = \sqrt{T_{\text{obs}} \sum_i \int \left(\frac{S_{\text{GW}}^{\text{Cosmo}}}{S_{i,N}} \right)^2 df}, \quad (3.16)$$

where the integral is over the LISA frequency range and $S_{\text{GW}}^{\text{Cosmo}}$ is related to $h^2\Omega_{\text{GW}}^{\text{Cosmo}}$ as in Eq. (3.7) and $\Omega_{\text{GW}}^{\text{Cosmo}}$ represents $\Omega_{\text{GW}}^{\text{BPL}}$ and $\Omega_{\text{GW}}^{\text{DBPL}}$ depending on the particular case. For $S_{i,N}$, include experimental noises defined in Eqs. (3.8) and (3.9).⁶

We also perform a Fisher analysis, which corresponds to approximating the likelihood function \mathcal{L} to be Gaussian. The relation between $\Delta\chi^2$ and the Fisher information matrix is given by

$$\Delta\chi^2 = \sum_{i,j} F_{ij} \Delta x_i \Delta x_j, \quad (3.17)$$

where $\Delta x_i \equiv x_{i,\text{postulated}} - x_{i,\text{fiducial}}$ and i, j run over the set of parameters. The Fisher information matrix F_{ij} is given by

$$F_{ij}(\vec{x}_{\text{fiducial}}) = \sum_{\alpha=A,E,T} T_{\text{obs}} \int df \left. \frac{(\partial_{x_i} h^2\Omega_\alpha)(\partial_{x_j} h^2\Omega_\alpha)}{(h^2\Omega_\alpha)^2} \right|_{\vec{x}=\vec{x}_{\text{fiducial}}}, \quad (3.18)$$

where $h^2\Omega_\alpha = h^2\Omega_{\text{GW}}^{\text{Cosmo}} + h^2\Omega_{\text{GW}}^{\text{Ext}} + h^2\Omega_{\text{GW}}^{\text{Gal}} + h^2\Omega_{N,\alpha}$ is the sum of the SGWBs, the foregrounds, and the fractional energy density noise $h^2\Omega_{N,\alpha} = \sum_\nu 4\pi^2 f^3 S_\alpha^\nu / (3H_0^2)$ with $\nu = \text{TM}, \text{OMS}$. The sum runs over the TDI AET channels. The projected relative uncertainty on the reconstruction of the parameters is then obtained from the diagonal values of the inverse of the Fisher information matrix, $\Delta x_i / x_i = \Delta \ln x_i = \ln 10 \times \Delta \log_{10} x_i = \ln 10 \times \sqrt{(F^{-1})_{ii}}$. Such errors represent the uncertainty on a given parameter after marginalizing over all the others.

4 Reconstruction of the geometric parameters

In this section, we discuss the prospect for the parameter reconstruction by LISA in terms of the geometric parameters, for the three templates presented in Sec. 2. The geometric-parameter templates have the advantage of speeding up the likelihood exploration as their parametrisation does not feature degeneracies. On the other hand, their non-trivial connection to PT parameters might lead to exploration of unphysical parts of the parameter space.

4.1 Broken power law

We start with very strong transitions, discussed in Sec. 2.1, leading to a SGWB from bubble collisions or highly relativistic fluid shells described by the BPL spectrum in Eq. (2.4). We fix the exponents to the values in Tab. 1, so that the geometric parameters of the model are $\vec{\theta}_{\text{Cosmo}} = (\log_{10} h^2\Omega_b, \log_{10} f_b/\text{Hz})$. In this case, we report the LISA sensitivity to the geometric parameters using both Fisher and Bayesian analyses.

As an example of the results of these analyses, Fig. 3 depicts the expected 68 % and 95 % confidence intervals (for likelihood analysis) or credible intervals (for Bayesian analysis) (CIs) of a BPL signal from bubble collisions with a fiducial amplitude $h^2\Omega_b = 3 \times 10^{-12}$

⁶It is also possible to include the astrophysical foregrounds, most importantly the galactic noise from Eq. (3.11), as noise sources which would bring our SNR curves closer to reconstruction including foregrounds.

parameter	$\mu \pm \sigma$	parameter	$\mu \pm \sigma$
A	3 ± 0.6	$\log_{10}(h^2\Omega_{\text{Gal}})$	-7.84 ± 0.21
P	15 ± 3	$\log_{10}(h^2\Omega_{\text{Ext}})$	-12.38 ± 0.17

Table 2: Mean μ and standard deviation σ of the Gaussian priors used in `Polychord` for the noise parameters A and P as well as the amplitudes of the Galactic ($\log_{10}(h^2\Omega_{\text{Gal}})$) and extra-Galactic ($\log_{10}(h^2\Omega_{\text{Ext}})$) foregrounds. The injected values correspond to the mean.

parameter	prior range	parameter	prior range
$\log_{10}(h^2\Omega_b)$	$(-30, -5)$	$\log_{10}(h^2\Omega_2)$	$(-30, -5)$
$\log_{10}(f_b/\text{Hz})$	$(-7, 1)$	$\log_{10}(f_2/\text{Hz})$	$(-7, 1)$
		$\log_{10}(f_2/f_1)$	$(0, 2)$

Table 3: Ranges of the uniform priors used in `Polychord` for the parameters of the BPL (left) and DBPL (right). The spectral slopes are fixed to the values in Tab. 1 corresponding to the source under consideration.

and frequency $f_b = 1$ mHz. We have chosen these values as they provide a signal in the ballpark of the maximum sensitivity of LISA. The priors used for the noise and foreground parameters are listed in Tab. 2, while those for the SGWB parameters are listed in Tab. 3, left column. In addition to the signal reconstruction, Fig. 3 also shows the posteriors of the noise parameters A and P , as well as those of the amplitudes of the Galactic and extra-Galactic binary foregrounds, provided in Sec. 3.3. The outcome of the Fisher analysis is shown in red, whereas the blue contours depict the reconstruction using `Polychord`. The inlay in the upper right shows the corresponding SGWB and foreground spectra, as well as the instrument sensitivity. The dashed curves correspond to the injected spectrum, whereas the solid lines show the spectrum of the mean reconstructed parameters. The shaded areas depict the 68% and 95% CIs inferred from the spectra calculated from the parameter points in the posterior samples. The parameters of this example of signal are reconstructed with an accuracy within a few percent.

Let us now vary the values of the parameters f_b and Ω_b , and consider the corresponding reconstruction. The result is shown in Fig. 4. We display the relative uncertainty on the reconstructed values of the break amplitude $h^2\Omega_b$ (left) and frequency f_b (right) as a function of the fiducial values. The upper panel shows the result of the analysis when disregarding the foreground contributions, whereas the lower panel includes the expected foregrounds from unresolved Galactic and extra-Galactic binaries. The dark-red regions, delimited by solid lines, are reconstructed with an uncertainty of 1%, the intermediate regions delimited by long-dashed lines have a reconstruction uncertainty of 10%, whereas the light-red regions delimited by short-dashed lines are reconstructed within an order-one factor. For comparison, we again show the parameter estimation both from the Fisher analysis (in red), and with nested sampling, using the `Polychord` sampler (in blue). In

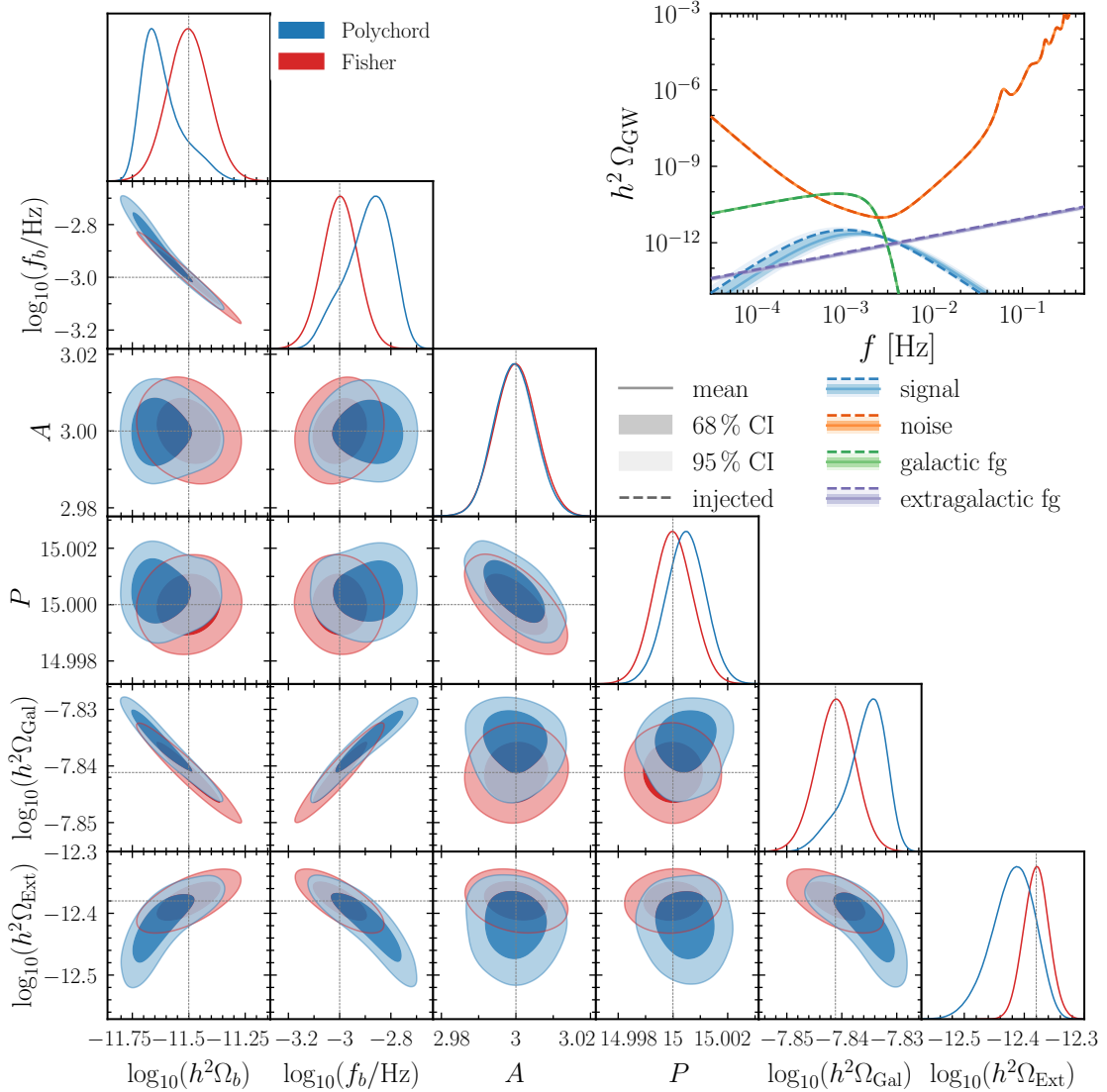


Figure 3: Triangle plot comparing the results of the Fisher analysis (red) and Polychord (blue) for a BPL spectrum corresponding to bubble collisions including noise and foregrounds. We fix the spectral exponents to the slopes for strong PTs in Tab. 1 and choose an injected signal with break frequency $f_b = 1$ mHz and amplitude $\log_{10}(h^2\Omega_b) = -11.5$. The plot in the top right corner visualizes the injected signals and noises as well as their reconstructed 68% (dark areas) and 95% (light areas) CIs obtained with Polychord.

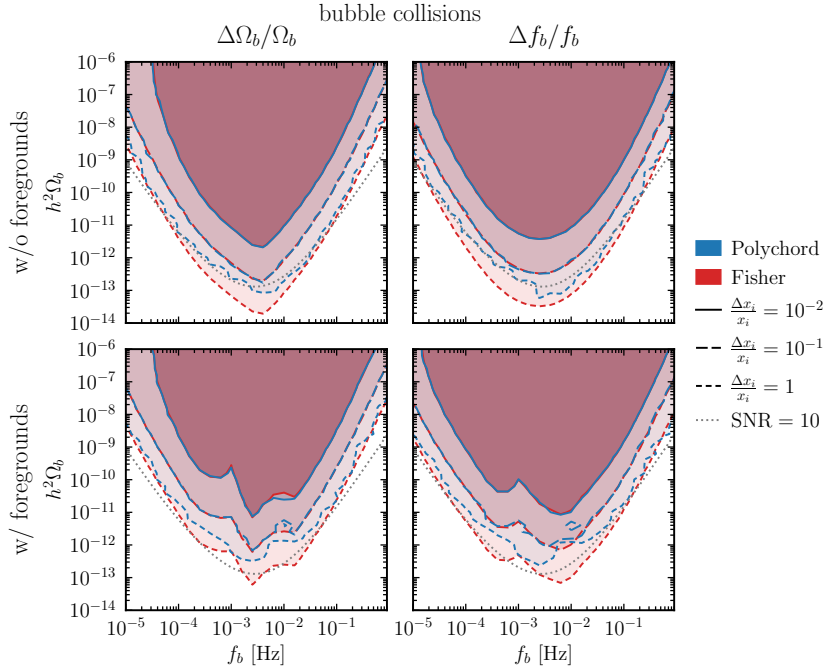


Figure 4: LISA sensitivity to the break frequency and amplitude of the BPL template using Fisher analysis (red) and `Polychord` (blue). The lower panel includes the foregrounds from Galactic and extra-Galactic binaries, whereas the upper panel is without foregrounds. The solid, long-dashed, and short-dashed lines correspond to a relative uncertainty of 1%, 10%, and 100% in the reconstruction of the amplitude Ω_b (left) and the frequency f_b (right), respectively. The gray dotted line indicates an SNR of 10 (neglecting foregrounds) in LISA.

the latter case, the relative uncertainty is calculated from the values of the diagonal of the covariance matrix of the `Polychord` samples, approximating the posterior as a normal distribution. The priors for the amplitude and break frequency are assumed to be uniform, with the corresponding ranges listed in Tab. 3. The parameters yielding an SNR of 10 are further indicated by the dotted gray line. We find that the uncertainty in the Fisher analysis agrees well with `Polychord` reconstruction in the region where the parameters are reconstructed within $\sim 10\%$ or better. Slight deviations can be seen in the region where the reconstruction works only at $\mathcal{O}(1)$. The highest sensitivity is achieved for break frequencies around $f_b \sim (10^{-3} - 10^{-2})$ Hz.

4.2 Double broken power law

Here we analyse the case of an SGWB generated by bulk fluid motion, discussed in Sec. 2.2, which can be described by the DBPL spectrum of Eq. (2.8). In this case, we report the LISA sensitivity to the geometric parameters using the Bayesian approach only.

The results for the DBPL are shown in Figs. 5 and 6. We reconstruct the geometric parameters $\vec{\theta}_{\text{Cosmo}} = \{\log_{10}(h^2\Omega_2), \log_{10}(f_2/\text{Hz}), \log_{10}(f_2/f_1)\}$ and calculate the uncertainty of the reconstructed values from the corresponding values of the covariance matrix. In Fig. 5, we adapt the DBPL spectrum to the sound waves case, setting the

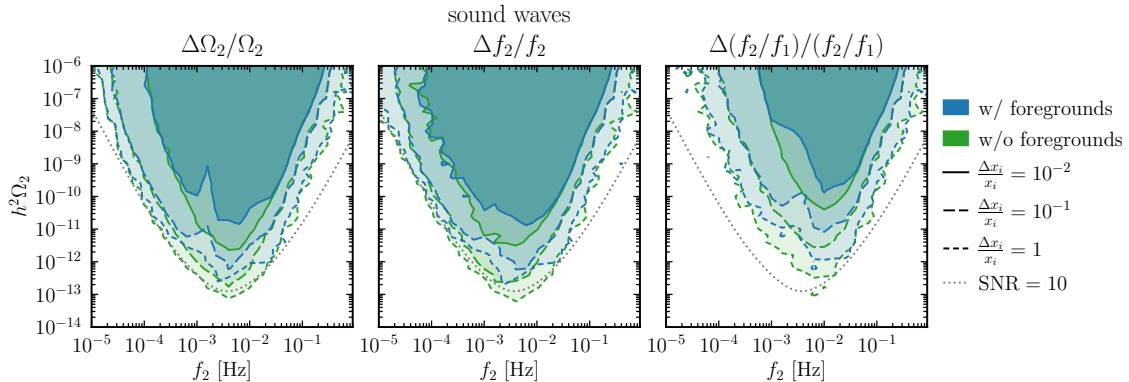


Figure 5: LISA sensitivity to the DBPL template parameters from Polychord. The blue regions correspond to the sensitivity including foregrounds, whereas the green curves only take into account the instrument noise. The fiducial point is taken from the sound wave template with $f_2/f_1 \simeq 2.5(\xi_w/\xi_{\text{shell}}) \approx 5.9$ corresponding to a detonation with $\xi_w \approx 1$ and $c_s = 1/\sqrt{3}$, see Eq. (2.9).

break frequency ratio to $f_2/f_1 \simeq 2.5(\xi_w/\xi_{\text{shell}}) \approx 5.9$, corresponding to a detonation with $\xi_w \approx 1$ and $c_s = 1/\sqrt{3}$, see Eq. (2.9). In Fig. 6, we adapt the DBPL spectrum to the MHD turbulence case, and by making use of Eq. (2.25) we set the frequency ratio to $f_2/f_1 \simeq 2.5\mathcal{N}\sqrt{R_*H_*}(F_{\text{GW},0}A_{\text{MHD}}/\Omega_2)^{1/4} \simeq 80(R_*H_*)^{1/2}(h^2\Omega_2/10^{-12})^{-1/4}$ for $\mathcal{N} = 2$. Note that, by expressing the amplitude of the SGWB in terms of Ω_2 in the case of MHD turbulence one introduces a spurious dependence of the ratio f_2/f_1 on R_*H_* , while physically it only depends on the fractional energy Ω_s . Therefore, in Fig. 6 we present the reconstruction for a few fixed values of R_*H_* . The priors used for the amplitude and break frequencies are listed in Tab. 3.

4.3 Synergy with other gravitational wave observatories

In Fig. 7, we compare the reconstruction reach of LISA to the one of next-generation ground-based GW interferometers, in particular the Einstein Telescope (ET) [149], and to the one of future PTAs, in particular the Square Kilometre Array (SKA) [150]. The black line depicts the parameters that produce an SNR of 10 in LISA after an effective observation time of four years. The red line indicates the parameters leading to an SNR of 10 in ET, using the noise curve from Ref. [151], whereas the orange line corresponds to the SKA, assuming observation of 1000 pulsars over 20 years with a timing cadence of two weeks and timing uncertainty of $0.1\ \mu\text{s}$ [152]. While synergies with ET are possible, simultaneous observation of a SGWB from a PT in the LISA and PTA bands requires unrealistically high amplitudes, due to the large separation between the frequency bands of the two experiments.

Another problem is the existence of foregrounds, which are not included in the SNR curves. The blue regions correspond to the respective reconstruction uncertainty estimated using Polychord including foregrounds in the LISA band (cf. Fig. 5), and a similar analysis

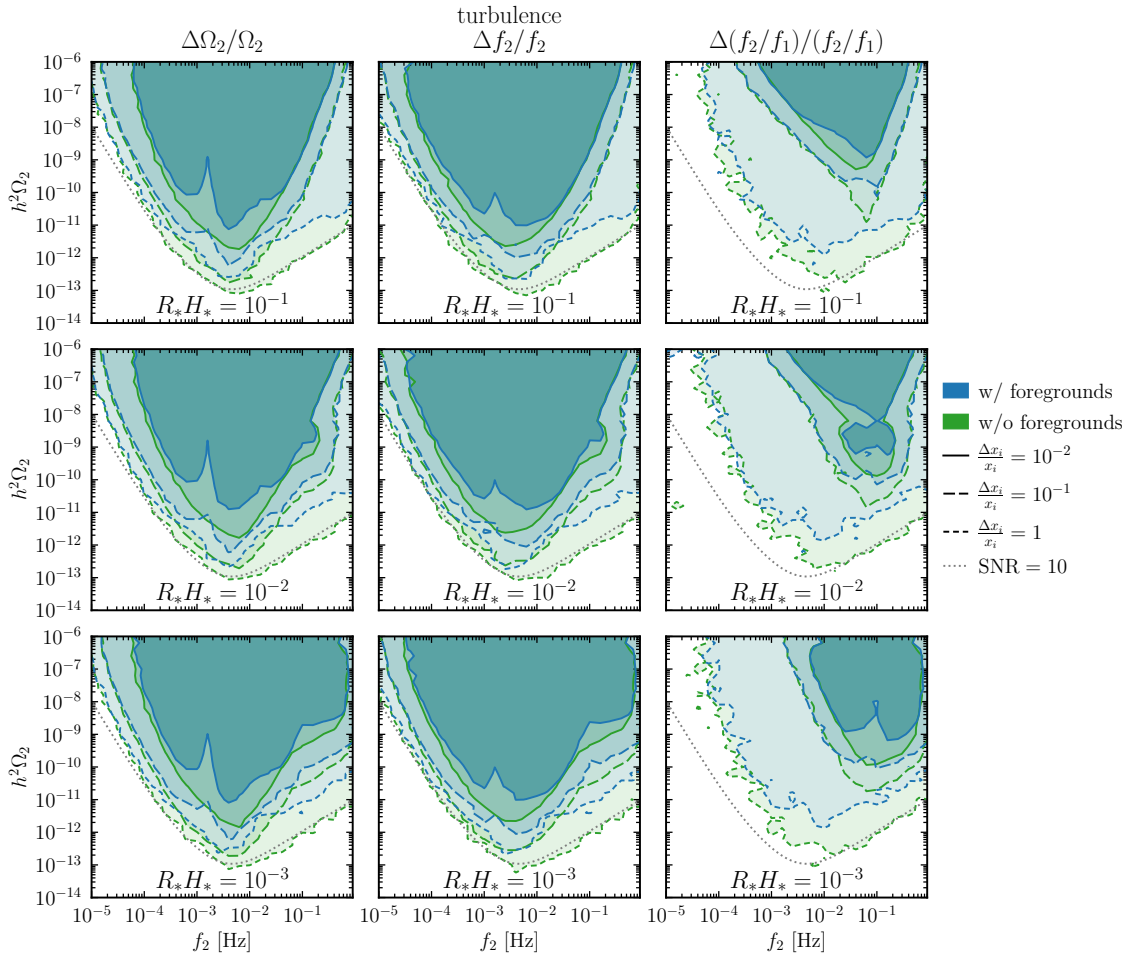


Figure 6: Same as Fig. 5. The fiducial point is taken from the turbulence template with $f_2/f_1 \simeq 80 (R_* H_*)^{1/2} (h^2 \Omega_2 / 10^{-12})^{-1/4}$, see Eq. (2.25). The rows correspond to different values of $R_* H_* = 10^{-1}$, 10^{-2} , and 10^{-3} .

would be required for the other experiments, which would further diminish the prospects for synergy between the experiments.

5 Reconstruction of the thermodynamic parameters

As shown in Sec. 2, the SGWB signal from a first-order PT can be expressed in terms of a set of thermodynamic parameters, depending on the sourcing process. The SGWB from bubble collisions or highly relativistic fluid shells in strong first-order PTs is determined by the energy fraction $\tilde{K} \approx 1$, the relative inverse PT duration β/H_* , and the temperature at the end of the PT, T_* . The bubble wall speed does not enter, since in this case the bubble walls move close to the speed of light, $\xi_w \simeq 1$. In the case of a SGWB generated by both sound waves and turbulence, the parameters entering the spectrum are rather connected to the bulk fluid motion: the kinetic energy fraction K , the relative size of the bulk fluid motion $H_* R_*$, and the PT temperature T_* . For sound waves, the fluid shell thickness,

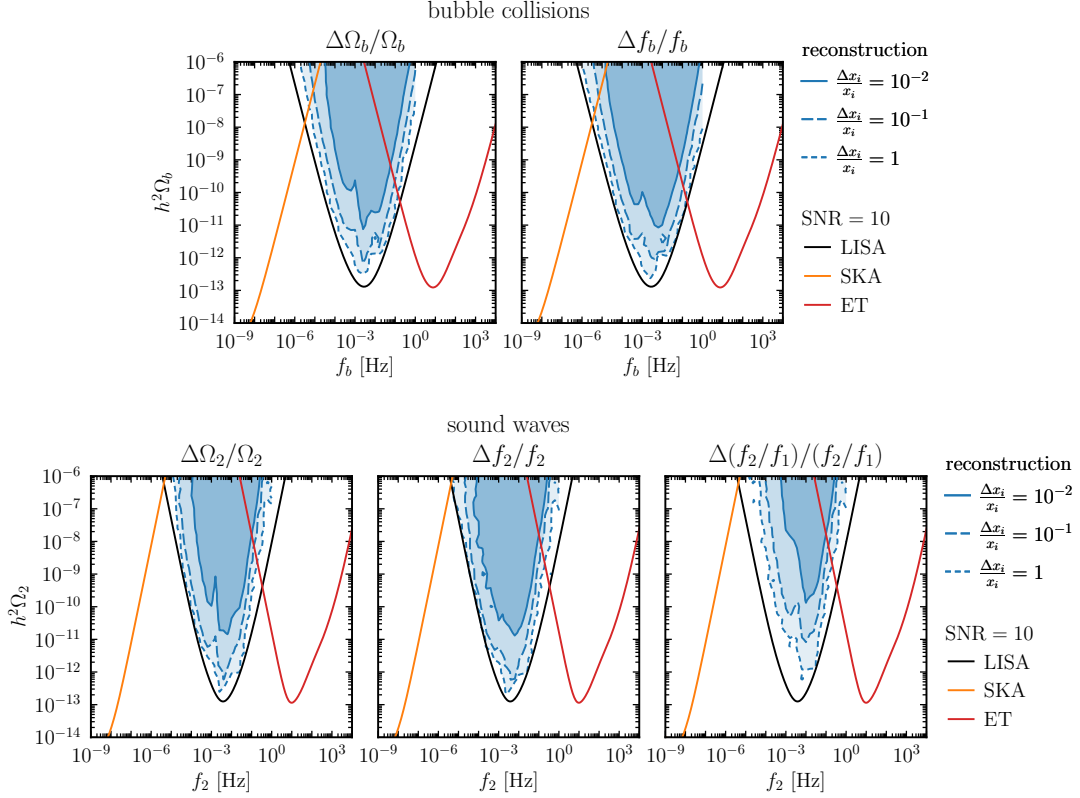


Figure 7: Relative uncertainty for the reconstruction of amplitude (left), frequency (top right or bottom center), and frequency ratio (bottom right, only for sound waves) in the cases of bubble collisions (top) and sound waves (bottom). The black (LISA), red (ET), and orange (SKA) lines correspond to an SNR of 10 for both templates.

which depends on the bubble walls speed ξ_w and on the sound speed c_s , also enters the SGWB spectral shape; while for turbulence, there is an extra parameter, ε , representing the fraction of kinetic energy which is vortical rather than compressional. Note that the gradient and/or kinetic energy fractions \tilde{K} and K can be related to the PT strength α , while the typical scale of the bulk fluid motion can be connected to the PT inverse duration β/H_* and the bubbles wall speed ξ_w (see Eq. (2.11)).

While the SGWB spectra can be described in terms of three to five thermodynamic parameters, depending on the source, only two or three geometric parameters are present: the amplitude, and one or two break frequencies, depending on whether the power law is doubly or singly broken, i.e. whether the signal stems from strong transitions or is generated via interactions with the plasma. We are hence confronted with degeneracies when intending to infer the PT parameters from the signal. We will demonstrate that these degeneracies can be lifted if more than one contribution is reconstructed.

In this section, we therefore develop two methods to reconstruct the thermodynamic parameters entering the SGWB signals, both based on parameter estimation with *Polychord* implemented in the *SGWBinner*. The first one consists in estimating the thermodynamic

parameters directly. While this is the straightforward way to perform the parameter reconstruction, it is associated with additional computational costs to resolve the degeneracies discussed above. We hence also employ a second method which consists in estimating the geometric parameters first, and then converting the reconstructed geometric parameters to the corresponding thermodynamic ones. As it does not suffer from degeneracies, running the geometric-parameter reconstruction as a first step is computationally more efficient. It further simplifies the reinterpretation of the results in the case that new simulations indicate a change in the interdependence of the geometric and thermodynamic parameters.

We apply the parameter transformation from geometric to thermodynamic parameters directly to each point in the samples generated with `Polychord`, discarding unphysical points that, for instance, yield $\xi_w > 1$ or $\tilde{K} > 1$. This automatically takes into account the Jacobian factor from the change of variables, as it is encoded in the density of parameter points in the samples. The resulting posterior, however, in principle differs from the posterior obtained via direct sampling, as different priors are used. These differences can be removed by using the induced prior [65], i.e. the prior obtained from transforming the prior of the thermodynamic parameters to geometric parameters, when sampling in terms of the geometric parameters. Alternatively, each parameter point can be assigned a weight given by the ratio of the prior on the thermodynamic parameters to the induced prior. In the following, though, we refrain from doing so. Comparing the two approaches hence corresponds to studying the thermodynamic parameter reconstruction for two different prior assumptions. As our priors are flat and relations between (the logarithms of) the parameters are mostly linear, the differences in priors are expected to have no significant effect.

Bubble collisions and highly relativistic fluid shells In this case we have three independent thermodynamic parameters (\tilde{K} , β/H_* , T_*) but only two geometric parameters: the break position and its amplitude (f_b , $h^2\Omega_b$). The reconstruction of the thermodynamic parameters hence inevitably suffers from degeneracies. Fixing either of the three parameters, the other two can be determined uniquely. In particular, as strong transitions in sectors that are in equilibrium with the SM plasma have $\alpha \gg 1$, fixing $\tilde{K} \sim \frac{\alpha}{1+\alpha} \approx 1$ allows for the reconstruction of β/H_* and T_* . Alternatively, as shown by Eq. (2.7), we can obtain constraints on the combinations $T_*\beta/H_* \approx 54 \text{ TeV } f_b/\text{mHz}$ and $\tilde{K}H_*/\beta \approx \sqrt{10^6 h^2\Omega_b}$.⁷

Figure 8 shows the reconstruction of the thermodynamic parameters of the SGWB spectrum from bubble collisions with $\tilde{K} = 1$, $\beta/H_* = 500$, and $T_* = 200 \text{ GeV}$. As discussed in Sec. 2.1, even though the spectrum we adopt in this work for bubble collisions was computed assuming $\tilde{K} \approx 1$, here we keep \tilde{K} as a free parameter. The blue contours in Fig. 8 depict the reconstruction directly in terms of the thermodynamic parameters. The degeneracies between the parameters are clearly visible. In addition, the red contours show the reconstruction using a sample in terms of the break frequency f_b and amplitude $\log_{10}(h^2\Omega_b)$ of the corresponding BPL. The respective priors used in `Polychord` are listed in Tab. 4. In order to obtain the three thermodynamic parameters from the two geometric parameters, for each point in the sample, a random value for the transition temperature

⁷Note that we fix $g_* = 106.75$ in these expressions.

parameter	input	prior range	parameter	input	prior range
$\log_{10}(\tilde{K})$	0.0	(-5, 0)	$\log_{10}(h^2\Omega_b)$	-11.5	(-30, -5)
$\log_{10}(\beta/H_*)$	2.7	(0, 5)	$\log_{10}(f_b/\text{Hz})$	-2.7	(-7, 1)
$\log_{10}(T_*/\text{GeV})$	2.3	(0, 8)			

Table 4: Input values and flat prior ranges for the injection and reconstruction of our bubble collisions benchmark spectrum in terms of the thermodynamic parameters (left) and the geometric parameters (right). The spectral slopes are set to $(n_1, n_2, a_1) = (2.4, -2.4, 1.2)$, see Tab. 1.

T_* was drawn according to the prior in Tab. 4, and the remaining parameters \tilde{K} and β/H_* have been calculated assuming this temperature.⁸ The green contours indicate the Fisher analysis estimate in terms of the geometric parameters, converted to thermodynamic parameters using the same method.

The three approaches yield consistent results for the parameter estimation. Note that in the particular case of the bubble collision spectrum, the priors in the two sampling methods are actually equivalent, as both methods use flat priors for $\log_{10}(T_*/\text{GeV})$, so that there are no differences induced by the temperature dependence of the effective degrees of freedom, and boundary effects from samples with parameters corresponding to unphysical values of $\log_{10}(\tilde{K})$ are avoided by discarding the corresponding parameter points.

Sound waves The SGWB spectrum from sound waves is given in terms of three geometric parameters, the two frequency breaks and the amplitude at the second break, but four thermodynamic parameters, K , H_*R_* , T_* , and ξ_w . The relation between the geometric parameters f_1 , f_2 , and Ω_2 in the sound waves template and the thermodynamic parameters are given in Eqs. (2.9), (2.10) and (2.12). In this case, the frequencies depend on H_*R_* , ξ_w , and T_* , and the integrated amplitude Ω_{int} on K and H_*R_* , while Ω_2 also involves ξ_w through the ratio f_2/f_1 (both amplitudes Ω_2 and Ω_{int} also depend subdominantly on T_* via the degrees of freedom). This allows us to reconstruct the thermodynamic parameters in the following way: from the ratio of the frequency breaks, $f_2/f_1 = 2.5 \Delta_w^{-1}(\xi_w)$ (see Eq. (2.9)), we can derive the compatible values of ξ_w (ξ_w might not be unique since $\Delta_w(\xi_w)$ is in general not invertible, so there can be one or two possible values of ξ_w for each Δ_w), from f_1 we can derive constraints (one for each value of ξ_w) on the ratio $T_*/(H_*R_*)$, and from the amplitude Ω_2 , combined with f_2/f_1 and f_1 , we can derive a constraint on a combination of K and T_* . These constraints are

$$\frac{T_*}{H_*R_*} \simeq 30 \text{ TeV} \frac{f_1}{\text{mHz}} \quad \text{and} \quad \min \left[K^2 H_*R_*, \frac{2}{\sqrt{3}} K^{\frac{3}{2}} (H_*R_*)^2 \right] \simeq \frac{\Omega_{\text{int}}}{1.8 \times 10^{-6}}, \quad (5.1)$$

⁸This corresponds to adding $\log_{10}(T_*/\text{GeV})$ as an additional parameter to the set of geometric parameters, i.e. $\{\log_{10}(h^2\Omega_b), \log_{10}(f_b/\text{Hz})\} \rightarrow \{\log_{10}(h^2\Omega_b), \log_{10}(f_b/\text{Hz}), \log_{10}(T_*/\text{GeV})\}$. The likelihood in this parametrisation remains independent of T_* , so that the new posterior is simply given by the original posterior multiplied by the prior on the additional parameter.

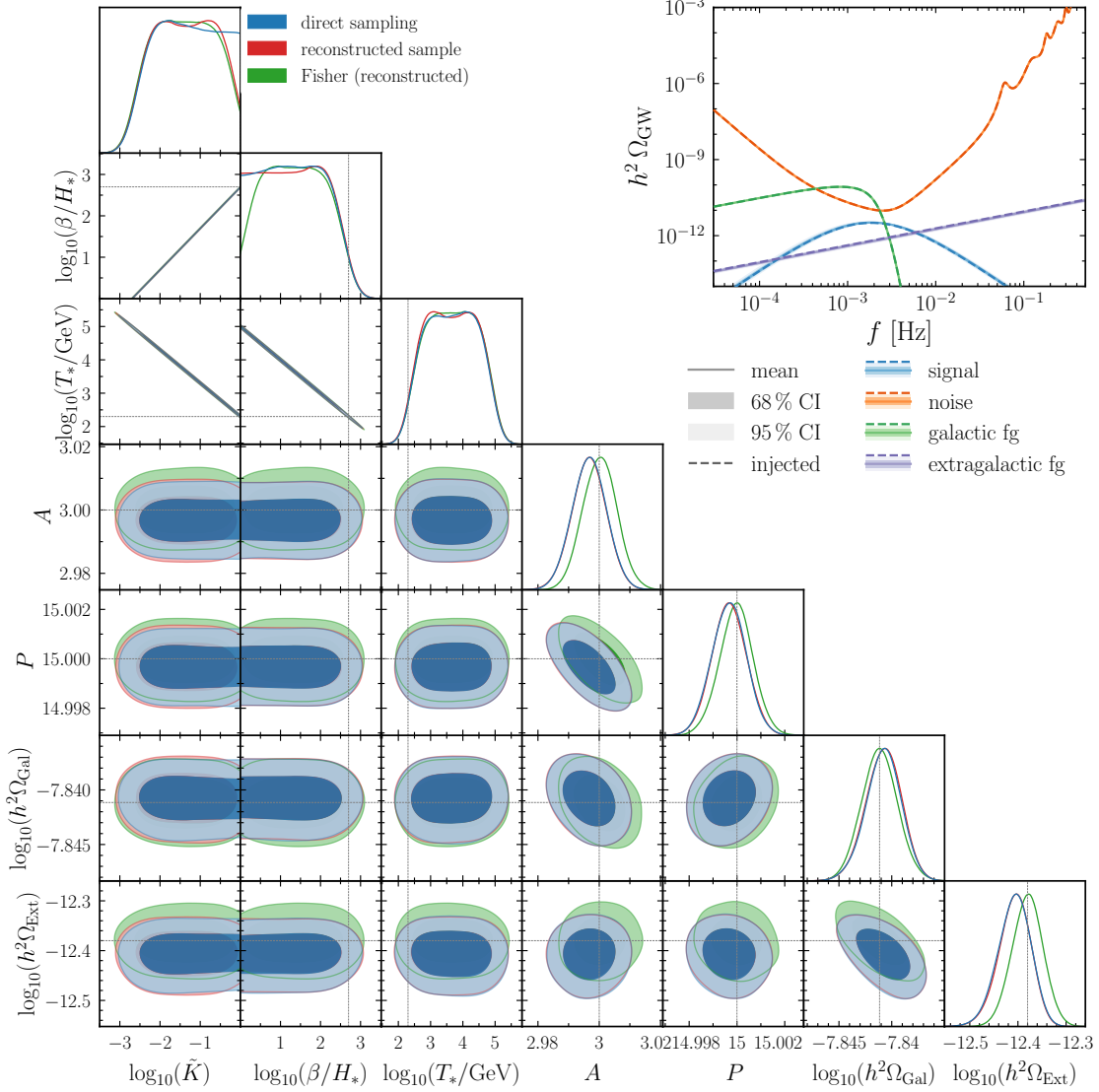


Figure 8: Reconstruction of the thermodynamic parameters of the GW spectrum from bubble collisions in a strong PT. The blue contours are sampled directly, whereas the red contour is reconstructed from a sample in terms of the geometric parameters of the BPL. The green contours are obtained from the Fisher analysis for the geometric parameters. The plot in the top right corner visualizes the injected signals and noises as well as the 68% (dark areas) and 95% (light areas) CIs of their reconstruction obtained from direct sampling.

where Ω_{int} is computed from f_2/f_1 and Ω_2 using Eq. (2.12). Hence, from the geometric parameters, we can only uniquely determine ξ_w (one or two values). The parameters H_*R_* and T_* are degenerate since only the ratio $T_*/(H_*R_*)$ is reconstructed (one constraint for each value of ξ_w) using Eq. (5.1). Furthermore, H_*R_* and K are also degenerate via Eq. (5.1). There are two possible degeneracies, due to the min function that appears in the computation of the sound wave time τ_{sw} (cf. discussion in Sec. 2.2.1). Hence, either the product $K^2H_*R_*$ or $K^{3/2}(H_*R_*)^2$ is constrained. Therefore, in general, the parameters K , H_*R_* , and T_* cannot be uniquely reconstructed from the geometric parameters of the sound waves template. However, the method described in the previous section and displayed in Fig. 8 can also be applied in this case.

Turbulence The geometric parameters f_1 , f_2 , and Ω_2 in the turbulence template are given in Eq. (2.25), and depend bijectively on Ω_s (from the ratio of the break frequencies), H_*R_* (from the amplitude), and T_* (via $H_{*,0}$ in f_1). This gives

$$\varepsilon K = \Omega_s \simeq \frac{6.5 \mathcal{N}^2}{(f_2/f_1)^2}, \quad (5.2a)$$

$$H_*R_* \simeq \frac{6 \times 10^{-4}}{\mathcal{N}^2} \left(\frac{f_2}{f_1}\right)^2 \sqrt{\frac{h^2 \Omega_2}{10^{-12}}}, \quad (5.2b)$$

$$T_* \simeq \frac{1.6 \text{ GeV}}{\mathcal{N}^2} \frac{f_2}{\text{mHz}} \left(\frac{f_2}{f_1}\right)^2 \sqrt{\frac{h^2 \Omega_2}{10^{-12}}}. \quad (5.2c)$$

Hence, from the geometric parameters we can determine uniquely H_*R_* and T_* , whereas K and ε are degenerate and only their product $\Omega_s = \varepsilon K$ is constrained.

Soundwaves + turbulence If we combine the SGWBs from sound waves and turbulence, $\Omega_{\text{GW}} = \Omega_{\text{GW}}^{\text{sw}} + \Omega_{\text{GW}}^{\text{turb}}$, and use the fit as a DBPL for each of the components, we can break the degeneracies present separately for the sound waves and turbulence and reconstruct all the thermodynamic parameters $\{K, H_*R_*, \xi_w, T_*, \varepsilon\}$ when the geometric parameters $\{f_1^{\text{sw}}, f_2^{\text{sw}}, f_1^{\text{turb}}, \Omega_2^{\text{turb}}, \Omega_2^{\text{sw}}\}$ can be inferred from the signal parameter estimation. Note that $f_2^{\text{turb}} = 2.2 H_{*,0}/(H_*R_*) \simeq 11 f_1^{\text{sw}}$, such that f_2^{turb} does not add information as long as we know its exact relation with f_1^{sw} . Indeed, one can see that given this relation, the first constraint in Eq. (5.1) and Eq. (5.2b) are equivalent if we use T_* from Eq. (5.2c).

From the sound waves geometric parameters we are able to reconstruct the possible value/s (one or two) of ξ_w from $f_2^{\text{sw}}/f_1^{\text{sw}}$, while we can reconstruct T_* from $\Omega_2^{\text{turb}}, f_1^{\text{turb}}$, and $f_1^{\text{sw}}/f_1^{\text{turb}}$ (see Eq. (5.2c)). We can solve for K for both cases in Eq. (5.1) and then check which solution also satisfies the corresponding condition on the sound wave lifetime. This could lead to one or two solutions for K . Then, for each solution of K , we can reconstruct $\varepsilon = \Omega_s/K$. In general, the reconstruction of the geometric parameters of a combined sound waves and turbulence template allows us to reconstruct all the thermodynamic parameters in a unique way.

Figure 9 depicts an example of parameter reconstruction in terms of the thermodynamic parameters of the PT featuring both the sound waves and the turbulence contributions. The blue contours correspond to directly sampling the thermodynamic parameters

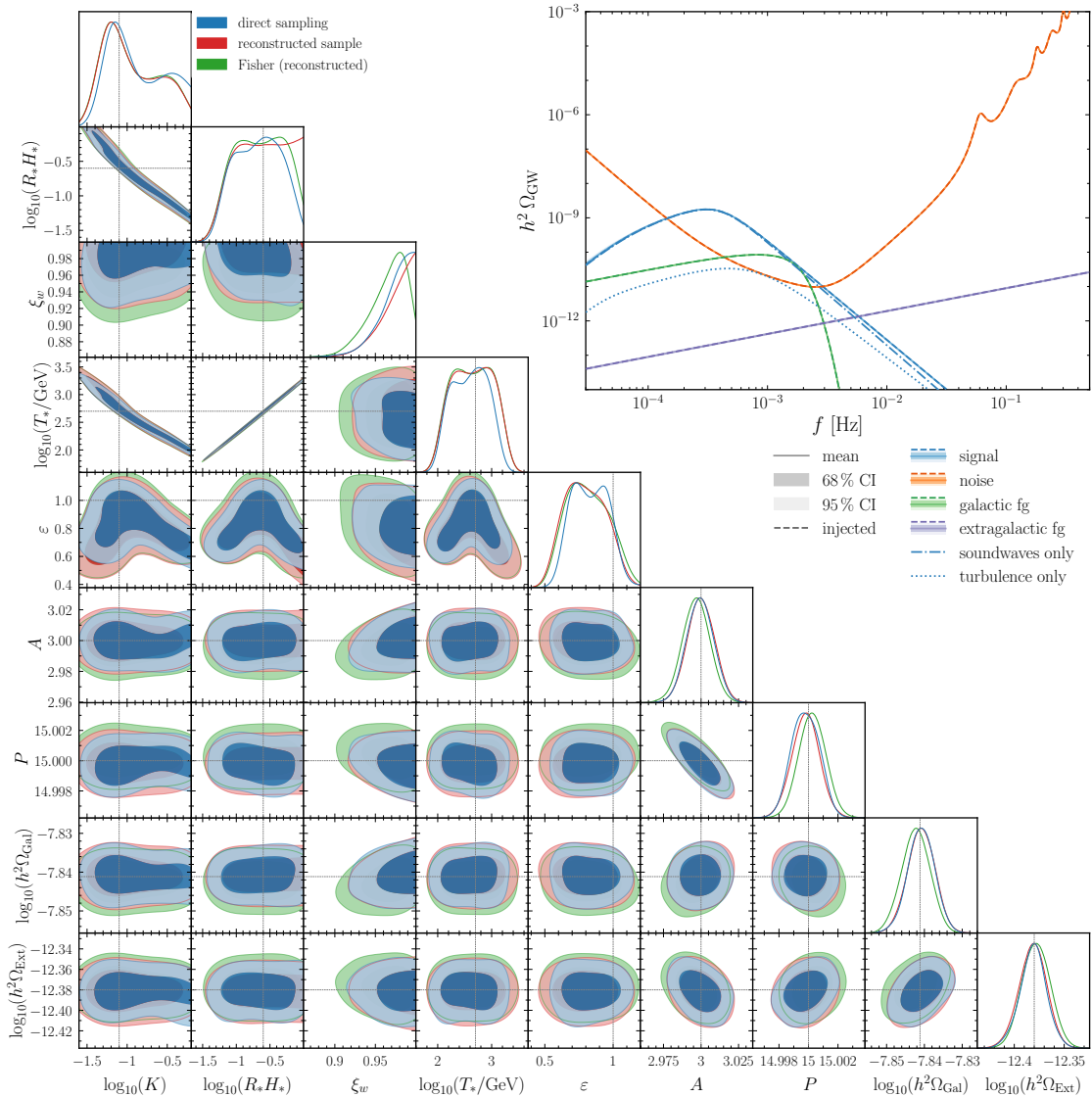


Figure 9: Reconstruction of the sum of the sound waves and turbulence SGWB spectra in terms of the thermodynamic parameters. The blue contours are sampled directly using Polychord in terms of the thermodynamic parameters, whereas the red contours are reconstructed from the sample in terms of the geometric parameters. The green contours are obtained from a Fisher analysis performed in terms of the geometric parameters.

parameter	input	prior range	parameter	input	prior range
$\log_{10}(K)$	-1.1	(-4, -0.2)	$\log_{10}(h^2\Omega_2^{\text{sw}})$	-8.8	(-30, -5)
$\log_{10}(R_*H_*)$	-0.6	(-3, 0)	$\log_{10}(\Omega_2^{\text{turb}}/\Omega_2^{\text{sw}})$	-1.7	(-5, 0)
ξ_w	1.0	(0.6, 1)	$\log_{10}(f_2^{\text{sw}}/\text{Hz})$	-3.4	(-5, -1)
$\log_{10}(T_*/\text{GeV})$	2.7	(0, 6)	$\log_{10}(f_2^{\text{sw}}/f_1^{\text{sw}})$	0.77	(0, 2)
ε	1.0	(0.01, 1.2)	$\log_{10}(f_1^{\text{turb}}/f_1^{\text{sw}})$	-0.21	(-2, 2)

Table 5: Input values and flat prior ranges for the injection and reconstruction of the turbulence plus sound waves benchmark spectrum in terms of the thermodynamic parameters (left) and of the geometric parameters (right). The ratio $f_2^{\text{turb}}/f_1^{\text{sw}}$ is fixed to 11 (cf. Eqs. (2.9) and (2.25)), whereas the spectral slopes are set to $(n_1, n_2, n_3, a_1, a_2) = (3, 1, -3, 2, 4)$ and $(n_1, n_2, n_3, a_1, a_2) = (3, 1, -8/3, 4, 2.15)$ for the sound waves and turbulence SGWB spectrum, respectively (cf. Tab. 1).

in **Polychord**. For the red contours, instead, we first sample over the geometric parameters and then convert the chains in terms of the thermodynamic parameters with the procedure previously described. Parameter points corresponding to unphysical values (ξ_w , K , or $R_*H_* > 1$) were discarded. The priors of the signal parameters in both cases are taken as uniform, with the corresponding ranges and the input values listed in Tab. 5. In addition, the green contours depict the result of the Fisher approach calculating the Fisher matrix in terms of the geometric parameters, creating samples using a multivariate Gaussian distribution according to the Fisher matrix, and then converting these to the thermodynamic parameters. While these approaches in principle differ in terms of the priors as discussed above, we again obtain consistent results.

Although in theory, the reconstruction of the sum of the two spectra should be unique, we can still see degeneracies between the kinetic energy fraction K , the bubble size R_*H_* , and the temperature T_* . These degeneracies arise since the first frequency break of the turbulence SGWB spectrum is hidden below the sound waves signal and the Galactic foreground, such that it cannot be reconstructed with enough precision. The corresponding loss of information inhibits the full reconstruction of the two spectra, leading to degeneracies, as one now needs to constrain five thermodynamic parameters from only four reconstructed geometric parameters. Furthermore, the two possible solutions for K , corresponding to the case where the SGWB generated from sound waves is cut off by their lifetime or at the Hubble time, lead to a kink in the 2D posteriors involving K or ε .

As a cross-check, Fig. 10 shows the reconstruction of the geometric parameters, i.e. the amplitudes and break frequencies of the two DBPLs, for the same input signal. The blue region now corresponds to directly sampling over the geometric parameters, whereas the red region shows the geometric parameters calculated from the sampling in terms of the thermodynamic parameters. The green region depicts the result from Fisher analysis. Note that we clipped the samples of the geometric parameters by removing parameter points that would yield unphysical values of ξ_w , K , or R_*H_* when converted to thermodynamic parameters. While this would ideally be done directly in the priors or using other con-

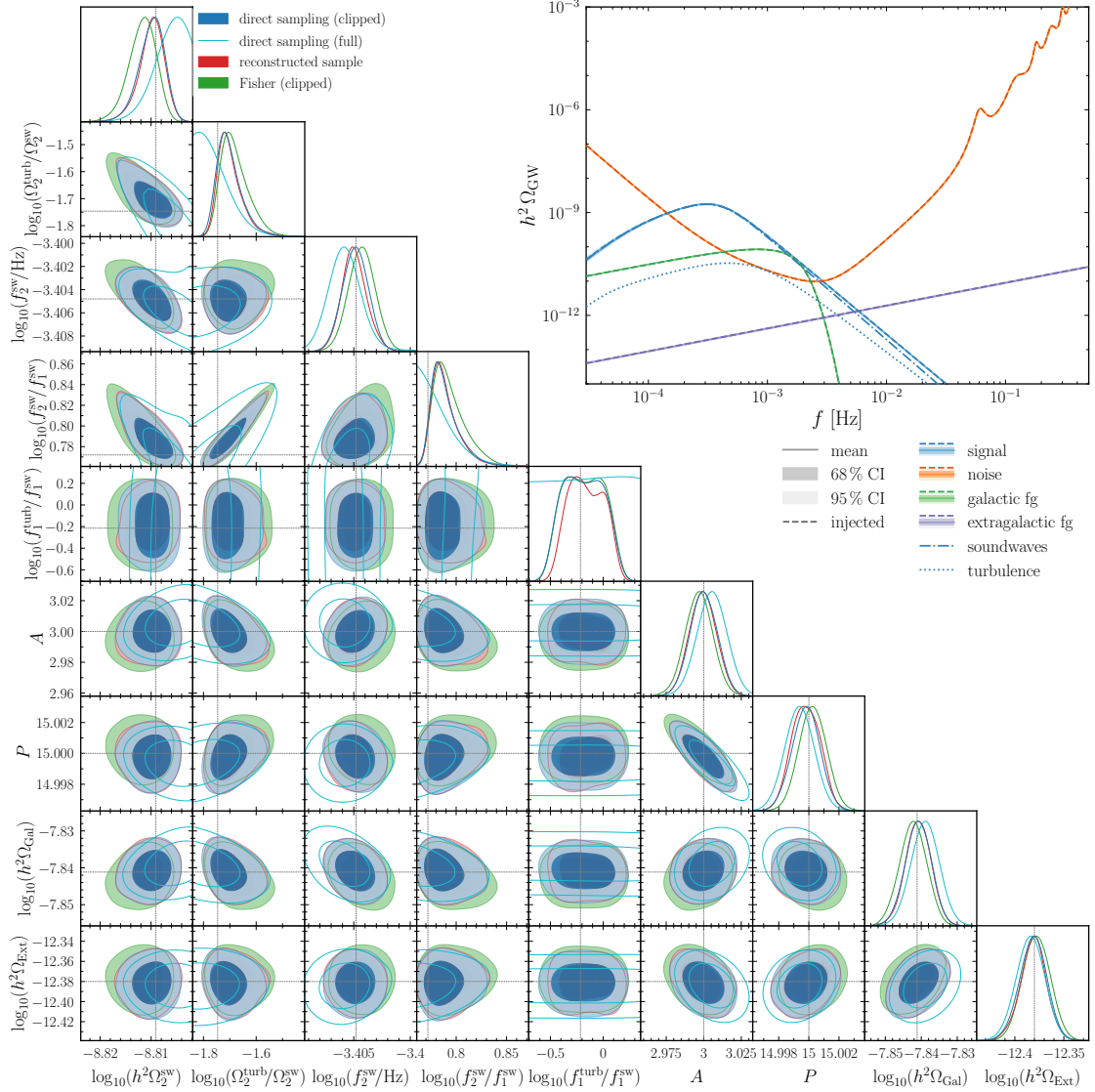


Figure 10: Reconstruction of the sum of two DBPLs in terms of the respective amplitudes and frequency breaks, assuming spectral slopes corresponding to the sum of the sound wave and turbulence spectra. The blue contours are sampled directly using Polychord, whereas the red contours are calculated from the sample in terms of the thermodynamic parameters. The green contours are obtained from Fisher analysis. Parameter points leading to unphysical thermodynamic parameters, i.e. ξ_w , K , or $H_*R_* > 1$ are discarded. These points are retained in the cyan contours.

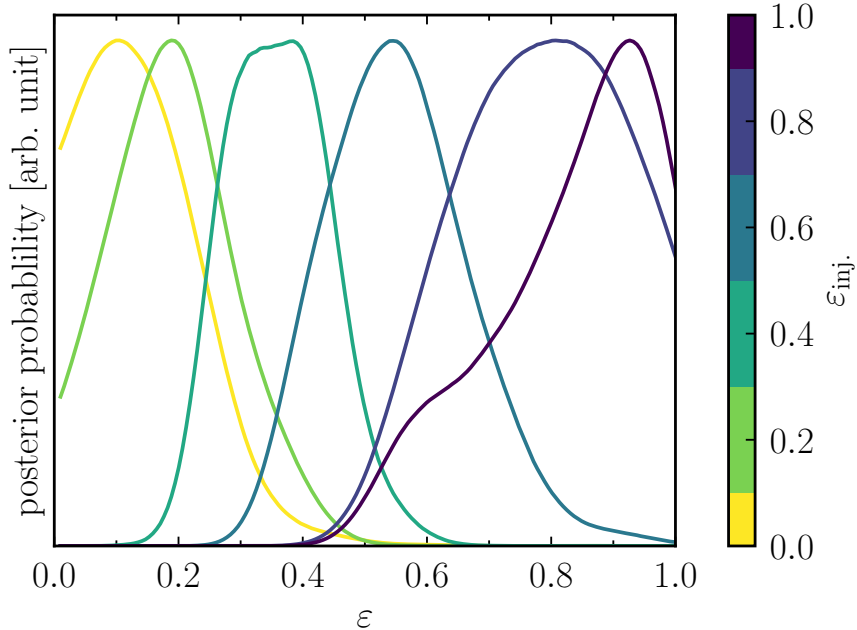


Figure 11: Posterior probability distributions for the reconstruction of ε using Polychord assuming $K = 0.08$, $H_*R_* = 0.25$, $\xi_w = 1$, and $T_* = 500$ GeV. The injected value of ε is varied between 0 and 1 in steps of 0.2.

straints, it turns out to be challenging to implement, due to the rather involved relations between the two sets of parameters (see, e.g., Ref. [65] for a possible implementation). For reference, we further include the unclipped results as cyan contours, where the failure of the reconstruction of f_1^{turb} , which leads to the degeneracies in the thermodynamic parameters reconstruction, becomes apparent.

Above we have treated the fraction ε of bulk kinetic energy converted to turbulent motion as an additional independent parameter in our set. However, in principle we expect ε to depend on the PT parameters and on the properties of the primordial plasma. Therefore, if determined independently from an observed GW signal from a PT in LISA, it would improve our understanding of the SGWB source. In Fig. 11, we hence depict the posteriors for the reconstruction of ε , where the colors indicate the injected value of ε . The remaining parameters are set to the ones listed in Tab. 5. While a precise determination of ε appears to be unrealistic, a strong SGWB signal from a PT can be used to at least roughly constrain the range of ε .

6 Interpretation in terms of fundamental particle physics models

In this section, we provide two examples of how the PT SGWB reconstruction can be recast as compelling bounds on the parameter space of particle physics models. Performing parameter inference starting from the LISA SGWB data directly on the parameters of a beyond the SM (BSM) Lagrangian is currently prohibitive. Indeed, computing the thermodynamic quantities governing the PT from the set of fundamental parameters within a given

model requires numerical tools [153–155] that, at the moment, are not ready for intensive, fast, automatised applications. For instance, numerical instabilities and the computation time can represent obstacles for likelihood samplers.

For our reconstruction, we use a simple approach that circumvents these issues. We begin by scanning the parameter space of the models on a regular grid, and for each point, we determine the thermodynamic parameters. Next, we interpolate the data to find the parameters as smooth functions of the fundamental parameters of the model. These are then ready to be used in the reconstruction of the SGWB signal at LISA. We then map our reconstruction back onto the model parameter space. We do so for a handful of benchmarks of the SGWB spectrum, appropriately chosen so that the geometrical parameters of the SGWB can be well reconstructed.

We now proceed to explain how the PT parameters can be calculated from the models we consider. Below the critical temperature T_c the new minimum in the potential of the theory becomes deeper than the initial one. From that moment the probability that the field tunnels into the new minimum due to thermal fluctuations can be approximated by [156, 157]

$$\Gamma(T) = \left(\frac{S_3(T)}{2\pi T} \right)^{\frac{3}{2}} T^4 e^{-S_3(T)}, \quad (6.1)$$

where $S_3(T)$ is the action of the field configuration driving the decay. The field configuration is obtained by solving the equation of motion of the field in a given potential assuming $O(3)$ -symmetry as appropriate for thermal systems. The probability of a point to remain in the initial vacuum is given by [158]

$$P(t) = \exp \left[-\frac{4\pi}{3} \int_{t_c}^t dt' \Gamma(t') a^3(t') r^3(t, t') \right], \quad (6.2)$$

where the comoving radius of a bubble reads

$$r(t, t') = \int_{t'}^t \frac{\xi_w(\tilde{t})}{a(\tilde{t})} d\tilde{t}. \quad (6.3)$$

for a bubble with wall velocity $\xi_w(\tilde{t})$ growing up to time t and nucleated at t' . We assume the appropriate time to compute the thermodynamic quantities governing the GW production is percolation time, when bubbles collide to fill the volume (we assume instantaneous reheating after the transition). This moment can be approximated by $P(t_*) \approx 0.7$, which allows us to find the corresponding percolation temperature T_* . The strength of the PT is approximated as [35, 38]

$$\alpha \equiv \frac{1}{\rho_r} \left(\Delta V(T) - \frac{T}{4} \frac{\partial \Delta V(T)}{\partial T} \right) \Big|_{T=T_*}, \quad (6.4)$$

where $\Delta V(T)$ is the energy difference between the two coexisting minima, and ρ_r denotes the radiation energy density of the Universe. The inverse duration of the transition can be computed using the action of the solution

$$\frac{\beta}{H_*} \equiv T_* \frac{d}{dT} \left(\frac{S_3(T)}{T} \right) \Big|_{T=T_*}, \quad (6.5)$$

and related to the average bubble size via Eq. (2.11). Using the methods described in Refs. [159–163] we verify all the points of interest feature highly relativistic walls $\xi_w \approx 1$. In this case the efficiency factor reads [91]

$$\kappa = \frac{\alpha}{0.73 + 0.083\sqrt{\alpha} + \alpha}, \quad (6.6)$$

and with it, we have all the thermodynamic parameters needed to compute the SGWB spectrum from bubble collisions and highly relativistic fluid shells (see Sec. 2.1) as well as from sound waves (see Sec. 2.2.1).

We apply this procedure to two illustrative models, namely the SM supplemented with a neutral singlet, and the classically conformal $U(1)_{B-L}$ extension of the SM. The former model is arguably the simplest SM extension allowing a strong first-order electroweak transition, while the latter is one of the minimal extensions featuring a wide parameter region with a very supercooled PT. Both extensions have few free parameters, making the scan of their whole parameter space feasible.

6.1 Gauge singlet extension with \mathbb{Z}_2 symmetry

One of the simplest extensions of the SM giving rise to PTs is that of an extra scalar singlet under the SM gauge group endowed with a \mathbb{Z}_2 symmetry [161, 163–176]. The tree-level potential in this model is written as

$$V_{\text{tree}}(\Phi, s) = -\mu_h^2 \Phi^\dagger \Phi + \lambda (\Phi^\dagger \Phi)^2 + \mu_s^2 \frac{s^2}{2} + \frac{\lambda_s}{4} s^4 + \frac{\lambda_{hs}}{2} s^2 \Phi^\dagger \Phi, \quad (6.7)$$

where $\Phi = (G^+, (h + iG^0)/\sqrt{2})^T$ is the SM Higgs doublet while s is the singlet field. We consider a two-step transition where the singlet gets a non-zero vacuum expectation value at high temperature before the electroweak transition, and require that the global $T = 0$ minimum of the potential lies at the electroweak vacuum $(h, s) = (v, 0)$ with $v = 246$ GeV. As usual, the minimisation conditions allow us to relate $\lambda = \mu_h^2/v^2$, $\mu_h^2 = m_h^2/2$, and $\mu_s^2 = m_s^2 - \lambda_{hs}v^2/2$, where m_h and m_s are the masses of the Higgs boson and the scalar singlet. The model is therefore described by the singlet mass m_s and the quartic couplings λ_s and λ_{hs} .

For a given value of singlet quartic coupling λ_s , the parameter space consistent with a first-order PT has a *banana* shape in the plane of m_s – λ_{hs} , such that larger λ_{hs} values are required for larger values of m_s . This shape arises from the requirements that the electroweak vacuum is the global minimum of the potential at $T = 0$, which gives an upper bound on λ_{hs} , and that the singlet gets a non-zero vacuum expectation value before the electroweak transition, which gives a lower bound on λ_{hs} [173]. The strength of the transition is controlled only by the Higgs-portal coupling and larger λ_{hs} values yield stronger PTs. As the singlet mass increases and due to the *banana* shape of the parameter space, very large λ_{hs} values are required to produce sizable effects. Thus for sufficiently large m_s (≈ 600 GeV) one reaches the perturbativity limit of the model.

The prospects of detection at colliders have been explored in Refs. [172, 175]. For scalar singlet masses in the range $65 \text{ GeV} < m_s < 300 \text{ GeV}$ the testability of this model

by direct and indirect collider signatures is very limited and for this reason, it has been dubbed the *nightmare scenario* [172]. We restrict our attention to the parameter range $65 \text{ GeV} < m_s < 125 \text{ GeV}$ for which λ_{hs} remains well within the perturbativity limit. The simplified \mathbb{Z}_2 version of the model we consider also faces theoretical issues. Firstly, the entire parameter space capable of supporting a first-order PT predicts an amount of scalar dark matter (DM) which would already have been seen by direct detection experiments [175]. Secondly, this version predicts the presence of scalar domain walls before the electroweak transition which would influence the nature of the transition [177]. While this is a challenge when building self-contained models we can simply assume minimal changes that would not affect the transition we want to model in a significant way. We can easily add new particles coupled to the singlet which would destabilise the scalar DM and hide it from direct detection experiments while providing a DM candidate with a large enough abundance [178]. Adding even a very small \mathbb{Z}_2 breaking term would cause the domain walls to annihilate before the electroweak transition [179]. Thus the problems of the model can be fixed with minimal modifications that would not have a significant impact on the PT dynamics and our parameter reconstruction forecast.

We use the SGWB spectrum produced by the sound waves source (see Sec. 2.2.1) as our benchmark for this model, further choosing $h^2\Omega_2 = 10^{-11}$ and $f_2 = 0.4 \text{ mHz}$. We do not include the signal from MHD turbulence since no analysis so far has been able to predict the value of ε . We implement a modified version of the `CosmoTransitions` code [153] to scan the parameter space of this model. The reconstruction of the SGWB spectrum with LISA is shown in Fig. 12. The corresponding area translated into the parameter space of the model, using the `ChainConsumer` package [180], is shown in Figs. 13 to 15. The first one indicates the parameter space in terms of the scalar mass m_s and portal coupling λ_{hs} while the dependence on the scalar quartic is shown using three benchmark values $\lambda_s = 0.1, 0.5$, and 1 to indicate its impact. Figure 14 shows the entire parameter space populated by first-order PTs by the singlet model for a fixed value of the quartic $\lambda_s = 1$ with the red ellipsis indicating the reconstruction of our SGWB benchmark point. The future experimental sensitivities are shown as violet lines and these correspond to Higgs associated production σ_{Zh} , vector boson fusion (VBF) at a Future Circular Collider (FCC) and the high luminosity Large Hadron Collider (LHC) [56, 181]. Figure 15 again shows the entire parameter space populated by first-order PTs by the singlet model in terms of the geometric parameters of the spectrum Ω_2 and f_2 (see Sec. 2.2.1) with the three panels using each of our three benchmark values $\lambda_s = 0.1, 0.5$, and 1 with the red ellipsis indicating the reconstruction of our benchmark point in each panel while the colour of points indicates the SNR of the corresponding spectrum.⁹

⁹Note that our formula for the SNR assumes a weak signal and very large values should be considered as qualitative indicators [182].

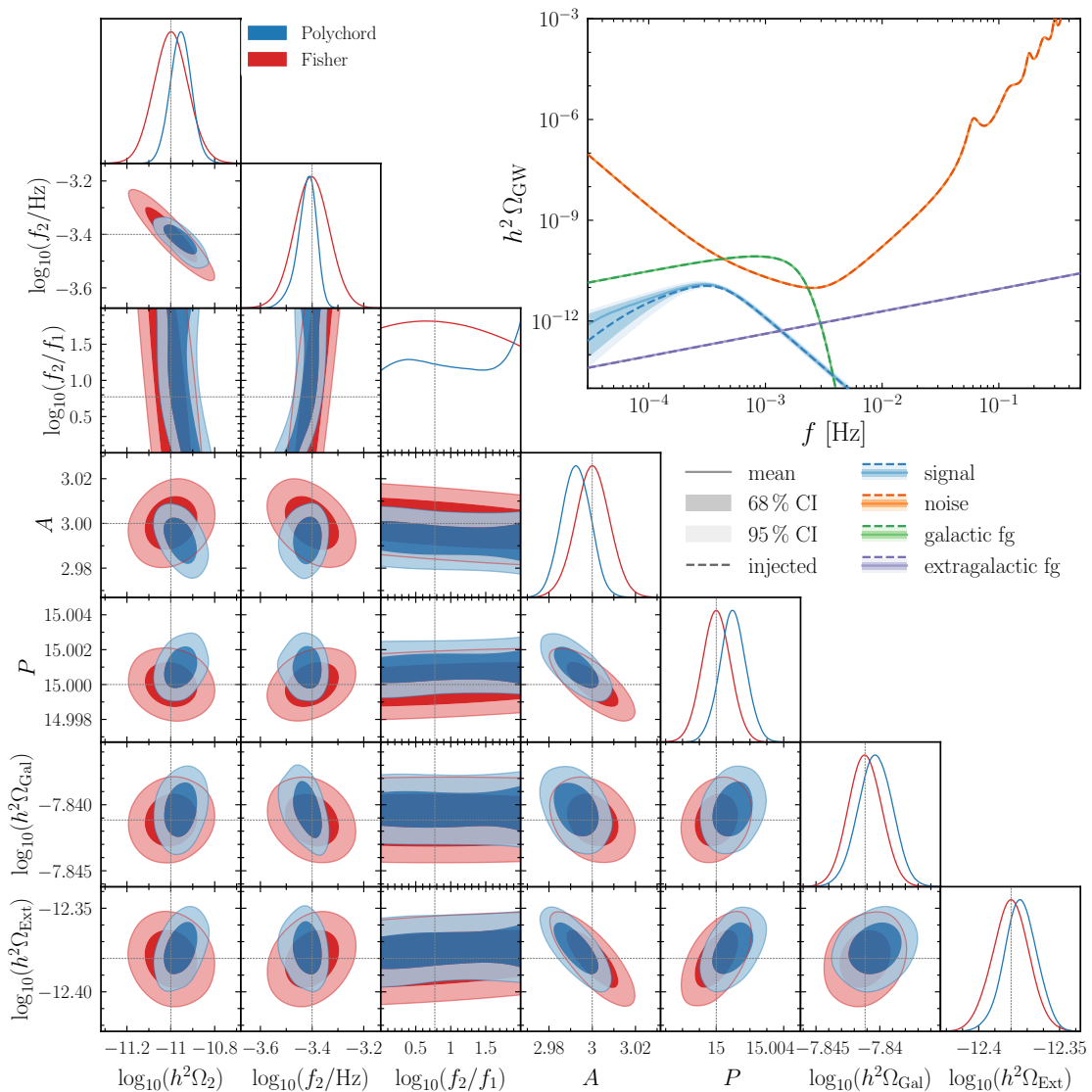


Figure 12: Reconstruction of the sound waves SGWB spectrum with $h^2\Omega_2 = 10^{-11}$ and $f_2 = 0.4\text{mHz}$, where the injected separation between the breaks $f_2/f_1 \approx 5.9$ is fixed by $\xi_w \approx 1$ (see Eq. (2.9)).

6.2 Classically conformal $U(1)_{B-L}$ model

The classically conformal $U(1)_{B-L}$ model [183–189] is characterised by the gauge symmetry $SU(3)_c \times SU(2)_L \times U(1)_Y \times U(1)_{B-L}$ and the scalar potential that at tree level is scale-invariant,

$$V = \lambda_H(H^\dagger H)^2 + \lambda_\phi(\phi^\dagger\phi)^2 - \lambda_p(H^\dagger H)(\phi^\dagger\phi), \quad (6.8)$$

where H is the Higgs $SU(2)_L$ doublet and ϕ is a complex scalar charged under $U(1)_{B-L}$. In addition to the SM parameters, this model includes three parameters: the $U(1)_{B-L}$ gauge coupling g_{B-L} , the $U(1)_{B-L}$ gauge boson mass $m_{Z'}$, and the gauge mixing parameter

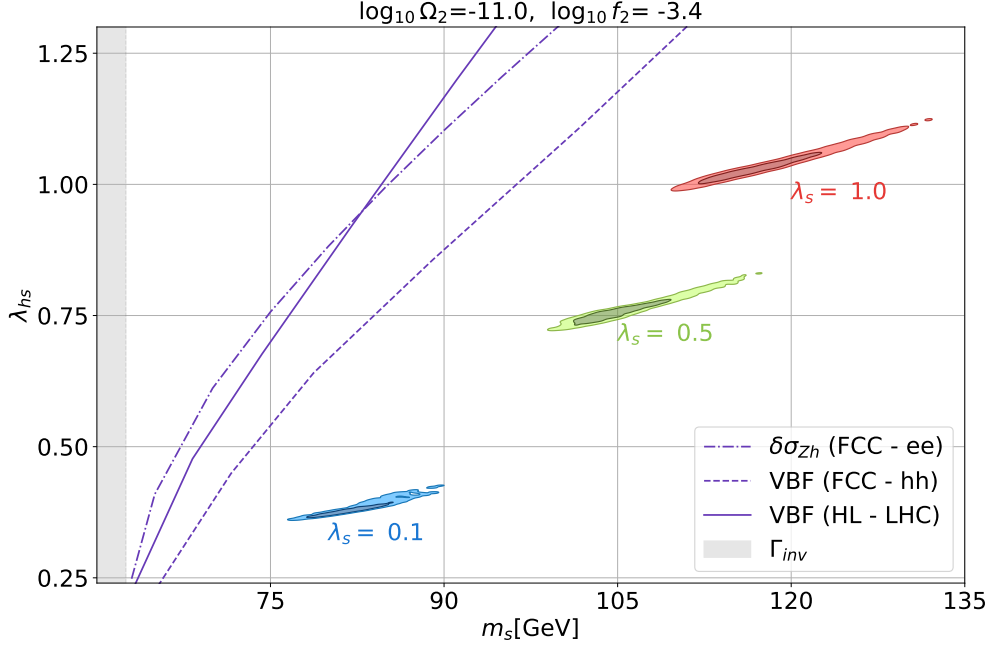


Figure 13: CIs for different values of singlet quartic couplings. The violet curves are experimental upper limits from the FCC and the high luminosity LHC. The gray shaded region is excluded by the Higgs invisible decay.

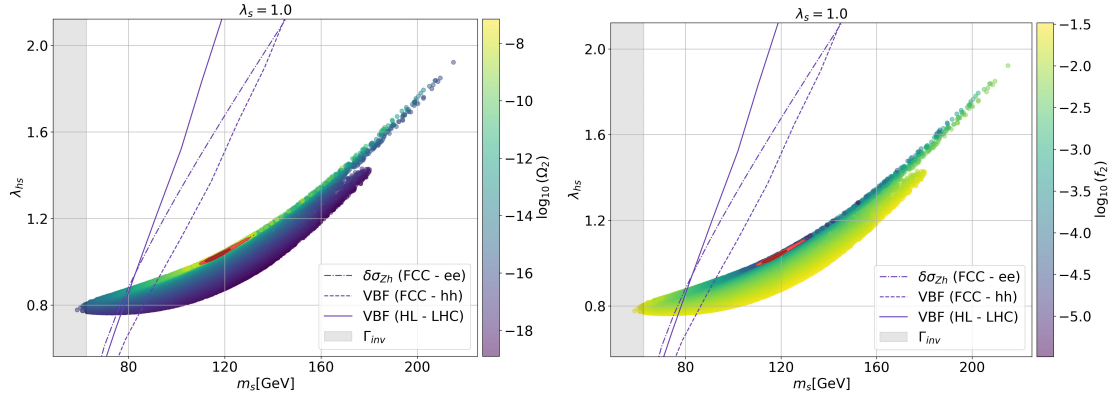


Figure 14: Parameter space of the singlet model. The colour bar displays the magnitude of the SGWB amplitude on the left panel and frequency on the right panel. The red region on top of the banana plots is the reconstructed ellipses.

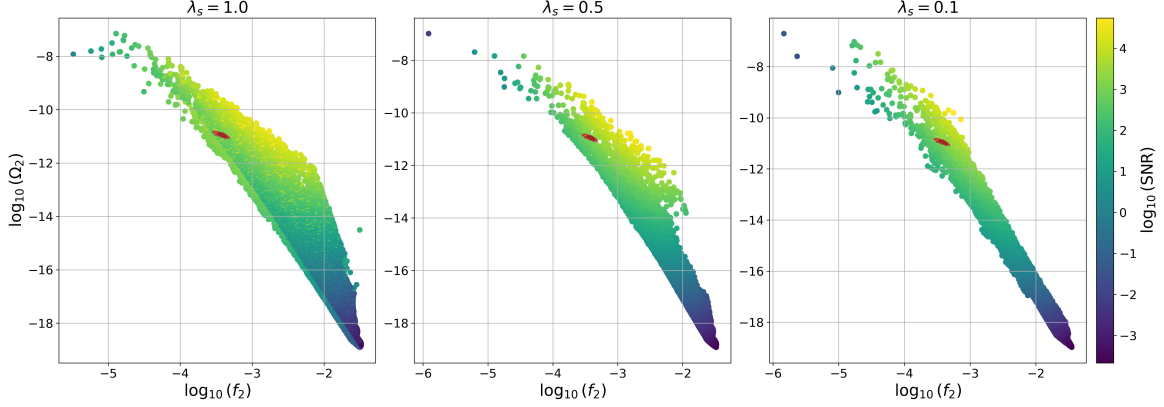


Figure 15: Geometric parameter space generated by the gauge singlet extension for different values of the singlet quartic coupling, displayed on top of each figure. The colour bar displays the SNR computed from the sound waves SGWB template. The small red ellipses on top of each plot are the CIs.

between $U(1)_Y$ and $U(1)_{B-L}$, \tilde{g} (all the quantities are computed at the renormalisation scale corresponding to the vacuum expectation value of ϕ). For $g_{B-L} \gtrsim 0.1$, which is the region relevant for the GW searches (see Fig. 18), collider searches exclude $m_{Z'} \lesssim 4 \text{ TeV}$ [190]. The PT dynamics is not very sensitive to the mixing parameter and we fix it to $\tilde{g} = -0.5$ that ensures perturbativity and vacuum stability of the model up to the Planck scale [187].

The PT dynamics and the resulting GW signal in this model have been studied, e.g. in Refs. [30, 185–189, 191, 192]. As typical for classically conformal models, the transition can be very strongly supercooled and, consequently, the GW signal arises from the bubble collisions and highly relativistic fluid shells.

We show the posteriors of the reconstruction in terms of the geometric parameters for two benchmark points with $h^2\Omega_b = 4 \times 10^{-12}$ and $f_b = 0.5 \text{ mHz}$, and $h^2\Omega_b = 6 \times 10^{-10}$ and $f_b = 0.2 \text{ Hz}$ in Fig. 16, and the corresponding posterior probability distributions in the model parameter space in Fig. 17. The first benchmark point, shown in the left panels, corresponds to a case where the peak of the SGWB spectrum is close to the best sensitivity of LISA and, consequently, the correlation in the reconstruction of Ω_b and f_b is small. This benchmark case is potentially within the reach of future collider experiments since the Z' gauge boson is not very heavy. For example, Ref. [187] estimated that the FCC could probe Z' masses up to 45 TeV [193].

The second benchmark point, shown in the right panel of Figs. 16 and 17, instead is at a much higher Z' mass and cannot be probed in colliders. In this case, the SGWB spectrum peak is in the high-frequency tail of the LISA sensitivity. Therefore, the reconstructed Ω_b and f_b are highly correlated. The SGWB spectrum in this case is, however, also in the reach of ET that will probe the opposite side of the GW spectrum than LISA, and combining these results will break the degeneracy in the reconstruction of Ω_b and f_b , consequently shrinking the posterior regions in the model parameter space. In Fig. 17, we show the

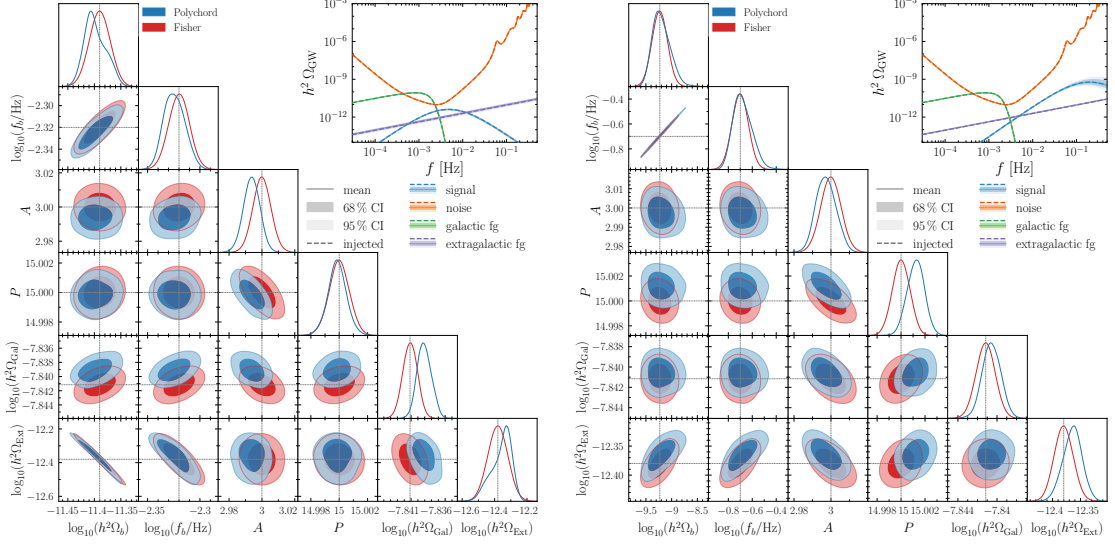


Figure 16: Reconstruction of the PT SGWB spectrum from bubble collisions and highly relativistic fluid shells with $h^2\Omega_b = 4 \times 10^{-12}$ and $f_b = 0.5$ mHz (left), and $h^2\Omega_b = 6 \times 10^{-10}$ and $f_b = 0.2$ Hz (right).

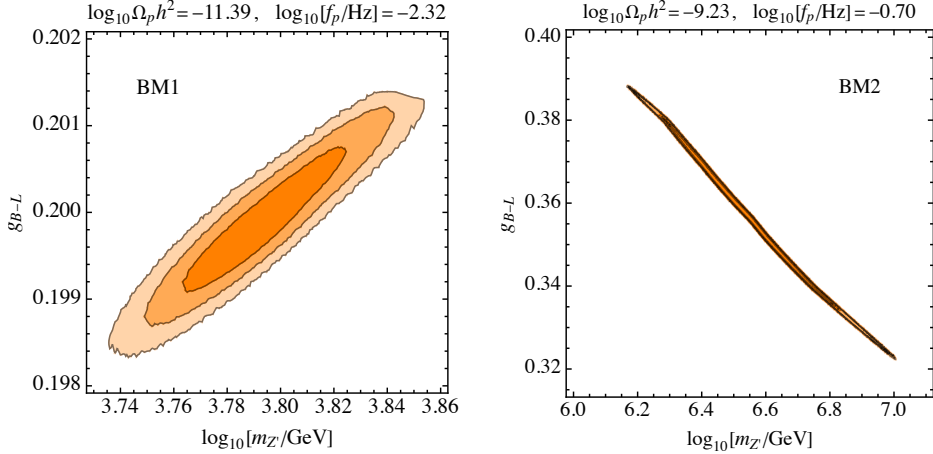


Figure 17: The shaded regions show the 68 %, 95 %, and 99.7 % CI regions of LISA in the $U(1)_{B-L}$ model parameter space for the bubble collisions SGWB signal (gauged $U(1)$ case) with the peak amplitude and frequency given above the plots.

peak amplitude and frequency of the SGWB spectrum and benchmark points on a broader range of the model parameters.

7 Conclusions

After the presence of an SGWB has been identified in the LISA data stream, an adequate interpretation of the SGWB origin must be based on templates, linking the frequency shape of the SGWB signal to the parameters of the sources. In the present and companion papers,

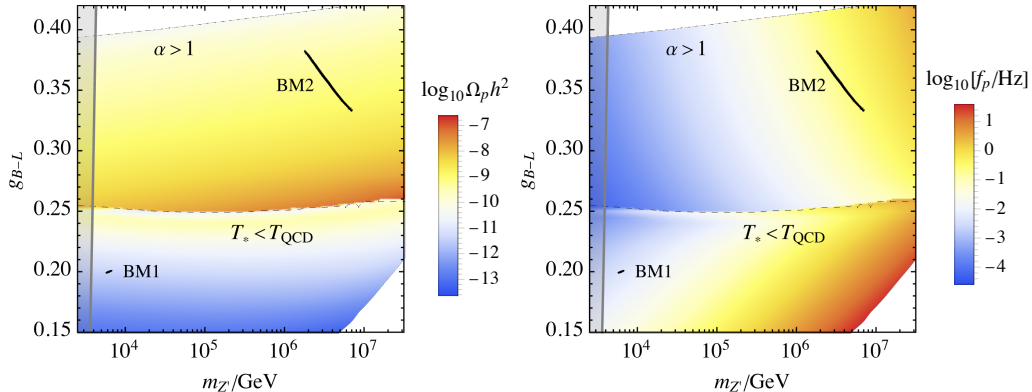


Figure 18: The colour coding shows in the left panel the peak amplitude and in the right panel the peak frequency of the SGWB spectrum in the $U(1)_{B-L}$ model. In the white region at the top, $\alpha < 1$. Below the dashed curve, the transition is triggered by the confinement of quantum chromodynamics (QCD) and the gray region on the left is excluded by collider searches of Z' .

focusing on cosmic strings [117] and phenomena linked to inflation [118], we have selected a set of SGWB templates suitable for this purpose, and prototyped the LISA template-based data analysis pipeline in `SGWBinner`, a code which has been used and tested for agnostic SGWB reconstructions in previous LISA-related analyses [115, 116]. We forecast the detection and reconstruction of these sources. Although developed under simplifying assumptions, this program allows us to identify and quantify the bottlenecks that the LISA community will have to tackle in the next years.

In the present paper, we have reported the PT-related part of the above program. As a first step, we have designed and implemented the templates for the main first-order PT mechanisms sourcing an SGWB, namely bubble collisions, sound waves and MHD turbulence. The former typically dominates the SGWB signal in BSM scenarios where the first-order PT is extremely strong, while the others emerge in the case of mid-strength transition scenarios (weak transitions rarely lead to an observable signal at current GW detectors). We have then adapted the `SGWBinner` to simulate data of the PT SGWB together with the astrophysical foregrounds and instrumental noises, and then forecast their parameter estimation. Crucially, the models used for the injection perfectly match the templates of the noise, astrophysical foregrounds, and SGWBs employed in the reconstruction. The forecasts then quantify the SGWB parameter estimation that LISA will perform if, at the time LISA flies, the community will have shrunk the theoretical and experimental uncertainties below the statistical errors reconstructed in our analysis. In this sense, all our templates, although representing the current state of the art combining simplicity and accuracy, must be understood as placeholders of the precise templates that the community is urged to build in the next decade. On the other hand, our qualitative results are not expected to change if, as expected, the future templates will be similar to the current ones.

We have performed an analysis of detection prospects as a function of the SGWB template parameters, showing that for signals peaking around 3 mHz, the relative errors (68 % CI) in the parameter reconstruction are around or below 10 % if the signal’s peak has an amplitude of $\Omega_p \gtrsim 10^{-12}$. This result, already remarkable on its own, does not leverage the yearly modulation of the Galactic foreground; if one optimistically assumes that this feature allows complete removal of this astrophysical foreground, the above-mentioned lower bound decreases to $\Omega_p \gtrsim 10^{-13}$. These two bounds have been obtained with the `SGWBinner` code accurately sampling the full likelihood. We have verified that the (fast and simple) Fisher approximation would lead to similar values for these two bounds. The observed tendency is that, in the reconstruction of the typical first-order PT signals, the values of the relative errors obtained with the Fisher approximation and with the full likelihood are in reasonably good agreement whenever they are about or below ten percent, while they quickly depart at higher values.

We have followed two approaches in the implementation of the first-order PT templates. In one case we have parameterised the templates in terms of parameters that describe the geometrical features of the SGWB signal frequency shape, i.e. the amplitude, frequency of the breaks, and the tilts of the spectrum. This parameterisation reduces the parameter degeneracies and, in turn, simplifies the sampling of the likelihood. In the second case, we have expressed the templates as a function of the thermodynamic parameters, describing the physics behind the signal such as the temperature of the transition, its duration, and the kinetic energy fraction. This implies parameter degeneracies but allows a more direct physics interpretation of the signal. For some benchmark signals with a satisfactory parameter reconstruction, we have verified that using the thermodynamic-parameter template leads to posteriors that are similar to those obtained by first using the geometric-parameter template and then converting the sampler chains into thermodynamic parameters. This is, however, only true provided one takes care to discard the regions corresponding to values of the geometric parameters leading to unphysical values for the thermodynamic ones.

The physics interpretation of the detection of (or upper bound on) the first-order PT SGWB cannot be limited to the thermodynamic parameters. Here we have proven that the SGWB reconstruction can lead to compelling bounds on particle physics models. Currently, performing parameter inference directly between a model Lagrangian and the LISA SGWB data is prohibitive, as calculating the PT (thermodynamic) parameters from a Lagrangian requires numerical tools that are not sufficiently automatised, fast or stable. We have shown how to circumvent the problem and applied the method to some concrete examples of BSM scenarios, namely the \mathbb{Z}_2 -singlet extension and the scale-invariant $U(1)_{B-L}$ extension. In the former model, with the detection of a first-order PT SGWB of amplitude $h^2\Omega_p \sim 10^{-11}$, LISA can constrain the singlet mass and the Higgs-singlet coupling with an accuracy of about ten percent (for a known singlet quartic coupling). In the latter model, with a similar first-order PT SGWB detection, LISA could bind the new gauge coupling with a relative error of one percent. The synergy with current and future particle physics experiments is manifest.

The synergy with other GW detectors is instead less clear. We have found that the joint detection of the same first-order PT signal both at LISA and SKA is unlikely. The

prospects are more optimistic with ET. The observation in both LISA and ET would require first-order PT signals with a peak frequency at $f_p \sim 0.1$ Hz, and peak amplitude $\Omega_p \gtrsim 10^{-10}$ for a vacuum-dominated transition and $\Omega_p \gtrsim 10^{-9}$ for sound waves and turbulence. This signal would indicate particle physics scenarios with a symmetry scale quite above the electroweak one. However, our synergy estimates with SKA and ET are likely optimistic, as they derive from SNR computations that do not account for technical limitations such as the presence of foregrounds in SKA and ET frequency bands. They can be considered as indicative of a possible synergistic detection of the first-order PT SGWB at SKA and ET, however, reaching robust conclusions would require dedicated studies.

In conclusion, the detection of the SGWB by LISA holds the potential for a historical, groundbreaking discovery. The precise reconstruction of this signal would further amplify the scientific impact of the observation. Our forecasts and their potential interpretations have highlighted this impact on scenarios featuring a first-order PT.

However, these results hinge on our simplifying assumptions concerning several theoretical and experimental issues. We assume that the data stream can be precisely cleaned from transient noise and signals. For the noise, foregrounds and SGWB, we use the same templates for the injection and reconstruction, meaning that we neglect the systematic errors due to the current theoretical and experimental uncertainties on the noise and signals. Thus, our results constitute an approximate upper bound for such systematic error: above this bound, the PT SGWB reconstruction will not be limited by the instrument itself but by the insufficient knowledge of its actual sensitivity, the theoretical understanding of the SGWB sources, and the data analysis capabilities. Ultimately, we intend this paper to serve as a call to action for the worldwide scientific community to address these challenges and unleash the full potential of LISA.

Acknowledgments

We acknowledge the LISA Cosmology Group members for seminal discussions. We especially thank the authors of Refs. [117, 118] for the collaborative developments of the `SGWBinner` code shared among this and those works. CC is supported by the Swiss National Science Foundation (SNSF Project Funding grant 212125). RJ is supported by JSPS KAKENHI Grant Numbers 23K17687 and 23K19048. The work of ML is supported by the Polish National Agency for Academic Exchange within the Polish Returns Programme under agreement PPN/PPO/2020/1/00013/U/00001 and the Polish National Science Center grant 2018/31/D/ST2/02048. EM acknowledges support from the Minerva foundation during the initial stage of the project. MM received support from the Swedish Research Council (Vetenskapsrådet) through contract no. 2017-03934. GN is partly supported by the grant Project. No. 302640 funded by the Research Council of Norway. MP acknowledges the hospitality of Imperial College London, which provided office space during some parts of this project. ARP is supported by the Swiss National Science Foundation (SNSF Ambizione grant no. 182044). VV is supported by the European Union’s Horizon Europe research and innovation program under the Marie Skłodowska-Curie grant agreement

No. 101065736, and by the Estonian Research Council grants PRG803, RVTT3 and RVTT7 and the Center of Excellence program TK202.

A Response functions

Here we report on the LISA response functions that `SGWBinner` adopts. Further details can be found in Ref. [61].

For our choice of TDI variables, the response functions R_{ii} appearing in Sec. 3.2 read

$$R_{ii}(f) = 16 \sin^2 \left(\frac{2\pi fL}{c} \right) \left(\frac{2\pi fL}{c} \right)^2 \tilde{R}_{ii}(f) \quad (\text{A.1})$$

with $i = \text{A, E, T}$. The factors $\tilde{R}_{ii}(f)$ enclose the geometry of the detector. Their full expression, which are implemented in `SGWBinner` [61], can be well approximated as [194]

$$\tilde{R}_{\text{AA}}(f) = \tilde{R}_{\text{EE}}(f) \simeq \frac{9}{20} \left[1 + 0.7 \left(\frac{2\pi fL}{c} \right)^2 \right]^{-1}, \quad (\text{A.2})$$

$$\tilde{R}_{\text{TT}}(f) \simeq \frac{9}{20} \left(\frac{2\pi fL}{c} \right)^6 \left[1.8 \times 10^3 + 0.7 \left(\frac{2\pi fL}{c} \right)^8 \right]^{-1}. \quad (\text{A.3})$$

Analogously, in the noise model of Sec. 3.2, the power spectra are given by

$$\begin{aligned} P_{N,\text{AA}}(f, A, P) = P_{N,\text{EE}}(f, A, P) = 8 \sin^2 \left(\frac{2\pi fL}{c} \right) \tilde{R}_{\text{AA}}(f) \\ \left\{ 4 \left[1 + \cos \left(\frac{2\pi fL}{c} \right) + \cos^2 \left(\frac{2\pi fL}{c} \right) \right] S_{\text{AA}}^{\text{TM}}(f, A) + \right. \\ \left. + \left[2 + \cos \left(\frac{2\pi fL}{c} \right) \right] S_{\text{AA}}^{\text{OMS}}(f, P) \right\}, \end{aligned} \quad (\text{A.4})$$

and

$$\begin{aligned} P_{N,\text{TT}}(f, A, P) = 16 \sin^2 \left(\frac{2\pi fL}{c} \right) \tilde{R}_{\text{TT}}(f) \left\{ 2 \left[1 - \cos \left(\frac{2\pi fL}{c} \right) \right]^2 S_{\text{TT}}^{\text{TM}}(f, A) + \right. \\ \left. + \left[1 - \cos \left(\frac{2\pi fL}{c} \right) \right] S_{\text{TT}}^{\text{OMS}}(f, P) \right\}, \end{aligned} \quad (\text{A.5})$$

where S_{ii}^{OMS} and S_{ii}^{TM} are defined in Eqs. (3.8) and (3.9) and are the same for any $i = \text{A, E, T}$. From Eq. (3.7), one can see that T_{ii}^{TM} and T_{ii}^{OMS} are the factors in front of the corresponding S_{ii}^{OMS} and S_{ii}^{TM} .

Acronyms

BPL broken power law

BSM beyond the SM

CGB Compact Galactic Binary

CI confidence interval (for likelihood analysis) or credible interval (for Bayesian analysis)

CMB cosmic microwave background	MHD magnetohydrodynamic
DBPL double broken power law	NSB neutron-star binary
DM dark matter	OMS optical measurement system
ESA European Space Agency	PT phase transition
ET Einstein Telescope	PTA Pulsar Timing Array
FCC Future Circular Collider	QCD quantum chromodynamics
GW gravitational wave	SGWB stochastic GW background
KAGRA Kamioka Gravitational Wave Detector	SKA Square Kilometre Array
LHC Large Hadron Collider	SM Standard Model
LIGO Laser Interferometer Gravitational Wave Observatory	SNR signal-to-noise ratio
LISA Laser Interferometer Space Antenna	SOBHB stellar-origin black hole binary
LVK LIGO/Virgo/KAGRA	TDI time delay interferometry
	TM test mass
	VBF vector boson fusion

References

- [1] LIGO SCIENTIFIC, VIRGO collaboration, *Observation of Gravitational Waves from a Binary Black Hole Merger*, *Phys. Rev. Lett.* **116** (2016) 061102 [[1602.03837](#)].
- [2] LIGO SCIENTIFIC, VIRGO collaboration, *GW151226: Observation of Gravitational Waves from a 22-Solar-Mass Binary Black Hole Coalescence*, *Phys. Rev. Lett.* **116** (2016) 241103 [[1606.04855](#)].
- [3] LIGO SCIENTIFIC, VIRGO collaboration, *GW170104: Observation of a 50-Solar-Mass Binary Black Hole Coalescence at Redshift 0.2*, *Phys. Rev. Lett.* **118** (2017) 221101 [[1706.01812](#)].
- [4] LIGO SCIENTIFIC, VIRGO collaboration, *GW170608: Observation of a 19-solar-mass Binary Black Hole Coalescence*, *Astrophys. J. Lett.* **851** (2017) L35 [[1711.05578](#)].
- [5] LIGO SCIENTIFIC, VIRGO collaboration, *GW170814: A Three-Detector Observation of Gravitational Waves from a Binary Black Hole Coalescence*, *Phys. Rev. Lett.* **119** (2017) 141101 [[1709.09660](#)].
- [6] LIGO SCIENTIFIC, VIRGO collaboration, *GWTC-1: A Gravitational-Wave Transient Catalog of Compact Binary Mergers Observed by LIGO and Virgo during the First and Second Observing Runs*, *Phys. Rev. X* **9** (2019) 031040 [[1811.12907](#)].
- [7] LIGO SCIENTIFIC, VIRGO collaboration, *GWTC-2: Compact Binary Coalescences Observed by LIGO and Virgo During the First Half of the Third Observing Run*, *Phys. Rev. X* **11** (2021) 021053 [[2010.14527](#)].
- [8] LIGO SCIENTIFIC, VIRGO collaboration, *GWTC-2.1: Deep extended catalog of compact binary coalescences observed by LIGO and Virgo during the first half of the third observing run*, *Phys. Rev. D* **109** (2024) 022001 [[2108.01045](#)].
- [9] KAGRA, VIRGO, LIGO SCIENTIFIC collaboration, *GWTC-3: Compact Binary Coalescences Observed by LIGO and Virgo during the Second Part of the Third Observing Run*, *Phys. Rev. X* **13** (2023) 041039 [[2111.03606](#)].

- [10] NANOGrav collaboration, *The NANOGrav 15 yr Data Set: Evidence for a Gravitational-wave Background*, *Astrophys. J. Lett.* **951** (2023) L8 [2306.16213].
- [11] EPTA collaboration, *The second data release from the European Pulsar Timing Array - I. The dataset and timing analysis*, *Astron. Astrophys.* **678** (2023) A48 [2306.16224].
- [12] D. J. Reardon et al., *Search for an Isotropic Gravitational-wave Background with the Parkes Pulsar Timing Array*, *Astrophys. J. Lett.* **951** (2023) L6 [2306.16215].
- [13] H. Xu et al., *Searching for the Nano-Hertz Stochastic Gravitational Wave Background with the Chinese Pulsar Timing Array Data Release I*, *Res. Astron. Astrophys.* **23** (2023) 075024 [2306.16216].
- [14] NANOGrav collaboration, *The NANOGrav 15 yr Data Set: Constraints on Supermassive Black Hole Binaries from the Gravitational-wave Background*, *Astrophys. J. Lett.* **952** (2023) L37 [2306.16220].
- [15] EPTA collaboration, *The second data release from the European Pulsar Timing Array: V. Implications for massive black holes, dark matter and the early Universe*, 2306.16227.
- [16] J. Ellis, M. Fairbairn, G. Hütsi, J. Raidal, J. Urrutia, V. Vaskonen et al., *Gravitational waves from supermassive black hole binaries in light of the NANOGrav 15-year data*, *Phys. Rev. D* **109** (2024) L021302 [2306.17021].
- [17] NANOGrav collaboration, *The NANOGrav 15 yr Data Set: Search for Signals from New Physics*, *Astrophys. J. Lett.* **951** (2023) L11 [2306.16219].
- [18] D. G. Figueroa, M. Pieroni, A. Ricciardone and P. Simakachorn, *Cosmological Background Interpretation of Pulsar Timing Array Data*, *Phys. Rev. Lett.* **132** (2024) 171002 [2307.02399].
- [19] L. Bian, S. Ge, J. Shu, B. Wang, X.-Y. Yang and J. Zong, *Gravitational wave sources for pulsar timing arrays*, *Phys. Rev. D* **109** (2024) L101301 [2307.02376].
- [20] J. Ellis, M. Fairbairn, G. Franciolini, G. Hütsi, A. Iovino, M. Lewicki et al., *What is the source of the PTA GW signal?*, *Phys. Rev. D* **109** (2024) 023522 [2308.08546].
- [21] E. Madge, E. Morgante, C. Puchades-Ibáñez, N. Ramberg, W. Ratzinger, S. Schenk et al., *Primordial gravitational waves in the nano-Hertz regime and PTA data — towards solving the GW inverse problem*, *JHEP* **10** (2023) 171 [2306.14856].
- [22] C. Caprini and D. G. Figueroa, *Cosmological Backgrounds of Gravitational Waves*, *Class. Quant. Grav.* **35** (2018) 163001 [1801.04268].
- [23] LISA COSMOLOGY WORKING GROUP collaboration, *Cosmology with the Laser Interferometer Space Antenna*, *Living Rev. Rel.* **26** (2023) 5 [2204.05434].
- [24] A. Kosowsky, M. S. Turner and R. Watkins, *Gravitational radiation from colliding vacuum bubbles*, *Phys. Rev. D* **45** (1992) 4514.
- [25] A. Kosowsky and M. S. Turner, *Gravitational radiation from colliding vacuum bubbles: envelope approximation to many bubble collisions*, *Phys. Rev. D* **47** (1993) 4372 [astro-ph/9211004].
- [26] S. J. Huber and T. Konstandin, *Gravitational Wave Production by Collisions: More Bubbles*, *JCAP* **09** (2008) 022 [0806.1828].

- [27] D. Cutting, M. Hindmarsh and D. J. Weir, *Gravitational waves from vacuum first-order phase transitions: from the envelope to the lattice*, *Phys. Rev. D* **97** (2018) 123513 [[1802.05712](#)].
- [28] D. Cutting, E. G. Escartin, M. Hindmarsh and D. J. Weir, *Gravitational waves from vacuum first order phase transitions II: from thin to thick walls*, *Phys. Rev. D* **103** (2021) 023531 [[2005.13537](#)].
- [29] M. Lewicki and V. Vaskonen, *Gravitational wave spectra from strongly supercooled phase transitions*, *Eur. Phys. J. C* **80** (2020) 1003 [[2007.04967](#)].
- [30] J. Ellis, M. Lewicki and V. Vaskonen, *Updated predictions for gravitational waves produced in a strongly supercooled phase transition*, *JCAP* **11** (2020) 020 [[2007.15586](#)].
- [31] M. Lewicki and V. Vaskonen, *Gravitational waves from colliding vacuum bubbles in gauge theories*, *Eur. Phys. J. C* **81** (2021) 437 [[2012.07826](#)].
- [32] M. Lewicki and V. Vaskonen, *Gravitational waves from bubble collisions and fluid motion in strongly supercooled phase transitions*, *Eur. Phys. J. C* **83** (2023) 109 [[2208.11697](#)].
- [33] M. Kamionkowski, A. Kosowsky and M. S. Turner, *Gravitational radiation from first order phase transitions*, *Phys. Rev. D* **49** (1994) 2837 [[astro-ph/9310044](#)].
- [34] C. Caprini et al., *Science with the space-based interferometer eLISA. II: Gravitational waves from cosmological phase transitions*, *JCAP* **04** (2016) 001 [[1512.06239](#)].
- [35] C. Caprini et al., *Detecting gravitational waves from cosmological phase transitions with LISA: an update*, *JCAP* **03** (2020) 024 [[1910.13125](#)].
- [36] M. Hindmarsh, S. J. Huber, K. Rummukainen and D. J. Weir, *Gravitational waves from the sound of a first order phase transition*, *Phys. Rev. Lett.* **112** (2014) 041301 [[1304.2433](#)].
- [37] M. Hindmarsh, S. J. Huber, K. Rummukainen and D. J. Weir, *Numerical simulations of acoustically generated gravitational waves at a first order phase transition*, *Phys. Rev. D* **92** (2015) 123009 [[1504.03291](#)].
- [38] M. Hindmarsh, S. J. Huber, K. Rummukainen and D. J. Weir, *Shape of the acoustic gravitational wave power spectrum from a first order phase transition*, *Phys. Rev. D* **96** (2017) 103520 [[1704.05871](#)].
- [39] D. Cutting, M. Hindmarsh and D. J. Weir, *Vorticity, kinetic energy, and suppressed gravitational wave production in strong first order phase transitions*, *Phys. Rev. Lett.* **125** (2020) 021302 [[1906.00480](#)].
- [40] M. Hindmarsh and M. Hijazi, *Gravitational waves from first order cosmological phase transitions in the Sound Shell Model*, *JCAP* **12** (2019) 062 [[1909.10040](#)].
- [41] R. Jinno, T. Konstandin and H. Rubira, *A hybrid simulation of gravitational wave production in first-order phase transitions*, *JCAP* **04** (2021) 014 [[2010.00971](#)].
- [42] R. Jinno, T. Konstandin, H. Rubira and I. Stomberg, *Higgsless simulations of cosmological phase transitions and gravitational waves*, *JCAP* **02** (2023) 011 [[2209.04369](#)].
- [43] A. Kosowsky, A. Mack and T. Kahniashvili, *Gravitational radiation from cosmological turbulence*, *Phys. Rev. D* **66** (2002) 024030 [[astro-ph/0111483](#)].
- [44] A. D. Dolgov, D. Grasso and A. Nicolis, *Relic backgrounds of gravitational waves from cosmic turbulence*, *Phys. Rev. D* **66** (2002) 103505 [[astro-ph/0206461](#)].

- [45] G. Gogoberidze, T. Kahniashvili and A. Kosowsky, *The Spectrum of Gravitational Radiation from Primordial Turbulence*, *Phys. Rev. D* **76** (2007) 083002 [0705.1733].
- [46] T. Kahniashvili, L. Campanelli, G. Gogoberidze, Y. Maravin and B. Ratra, *Gravitational Radiation from Primordial Helical Inverse Cascade MHD Turbulence*, *Phys. Rev. D* **78** (2008) 123006 [0809.1899].
- [47] C. Caprini, R. Durrer and G. Servant, *The stochastic gravitational wave background from turbulence and magnetic fields generated by a first-order phase transition*, *JCAP* **12** (2009) 024 [0909.0622].
- [48] A. Brandenburg, T. Kahniashvili, S. Mandal, A. Roper Pol, A. G. Tevzadze and T. Vachaspati, *Evolution of hydromagnetic turbulence from the electroweak phase transition*, *Phys. Rev. D* **96** (2017) 123528 [1711.03804].
- [49] P. Niksa, M. Schlexer and G. Sigl, *Gravitational Waves produced by Compressible MHD Turbulence from Cosmological Phase Transitions*, *Class. Quant. Grav.* **35** (2018) 144001 [1803.02271].
- [50] A. Roper Pol, S. Mandal, A. Brandenburg, T. Kahniashvili and A. Kosowsky, *Numerical simulations of gravitational waves from early-universe turbulence*, *Phys. Rev. D* **102** (2020) 083512 [1903.08585].
- [51] T. Kahniashvili, A. Brandenburg, G. Gogoberidze, S. Mandal and A. Roper Pol, *Circular polarization of gravitational waves from early-Universe helical turbulence*, *Phys. Rev. Res.* **3** (2021) 013193 [2011.05556].
- [52] A. Roper Pol, S. Mandal, A. Brandenburg and T. Kahniashvili, *Polarization of gravitational waves from helical MHD turbulent sources*, *JCAP* **04** (2022) 019 [2107.05356].
- [53] A. Roper Pol, C. Caprini, A. Neronov and D. Semikoz, *Gravitational wave signal from primordial magnetic fields in the Pulsar Timing Array frequency band*, *Phys. Rev. D* **105** (2022) 123502 [2201.05630].
- [54] P. Auclair, C. Caprini, D. Cutting, M. Hindmarsh, K. Rummukainen, D. A. Steer et al., *Generation of gravitational waves from freely decaying turbulence*, *JCAP* **09** (2022) 029 [2205.02588].
- [55] A. Roper Pol, A. Neronov, C. Caprini, T. Boyer and D. Semikoz, *LISA and γ -ray telescopes as multi-messenger probes of a first-order cosmological phase transition*, 2307.10744.
- [56] J. Ellis, M. Lewicki and J. M. No, *On the Maximal Strength of a First-Order Electroweak Phase Transition and its Gravitational Wave Signal*, *JCAP* **04** (2019) 003 [1809.08242].
- [57] J. Ellis, M. Lewicki and J. M. No, *Gravitational waves from first-order cosmological phase transitions: lifetime of the sound wave source*, *JCAP* **07** (2020) 050 [2003.07360].
- [58] A. Roper Pol, S. Procacci and C. Caprini, *Characterization of the gravitational wave spectrum from sound waves within the sound shell model*, *Phys. Rev. D* **109** (2024) 063531 [2308.12943].
- [59] LISA collaboration, *Laser Interferometer Space Antenna*, 1702.00786.
- [60] C. Caprini, D. G. Figueroa, R. Flauger, G. Nardini, M. Peloso, M. Pieroni et al., *Reconstructing the spectral shape of a stochastic gravitational wave background with LISA*, *JCAP* **11** (2019) 017 [1906.09244].

- [61] R. Flauger, N. Karnesis, G. Nardini, M. Pieroni, A. Ricciardone and J. Torrado, *Improved reconstruction of a stochastic gravitational wave background with LISA*, *JCAP* **01** (2021) 059 [[2009.11845](#)].
- [62] C. Gowling and M. Hindmarsh, *Observational prospects for phase transitions at LISA: Fisher matrix analysis*, *JCAP* **10** (2021) 039 [[2106.05984](#)].
- [63] F. Giese, T. Konstandin and J. van de Vis, *Finding sound shells in LISA mock data using likelihood sampling*, *JCAP* **11** (2021) 002 [[2107.06275](#)].
- [64] G. Boileau, N. Christensen, C. Gowling, M. Hindmarsh and R. Meyer, *Prospects for LISA to detect a gravitational-wave background from first order phase transitions*, *JCAP* **02** (2023) 056 [[2209.13277](#)].
- [65] C. Gowling, M. Hindmarsh, D. C. Hooper and J. Torrado, *Reconstructing physical parameters from template gravitational wave spectra at LISA: first order phase transitions*, *JCAP* **04** (2023) 061 [[2209.13551](#)].
- [66] R. Sharma, J. Dahl, A. Brandenburg and M. Hindmarsh, *Shallow relic gravitational wave spectrum with acoustic peak*, *JCAP* **12** (2023) 042 [[2308.12916](#)].
- [67] M. Hindmarsh, *Sound shell model for acoustic gravitational wave production at a first-order phase transition in the early Universe*, *Phys. Rev. Lett.* **120** (2018) 071301 [[1608.04735](#)].
- [68] R.-G. Cai, S.-J. Wang and Z.-Y. Yuwen, *Hydrodynamic sound shell model*, *Phys. Rev. D* **108** (2023) L021502 [[2305.00074](#)].
- [69] D. Croon, O. Gould, P. Schicho, T. V. I. Tenkanen and G. White, *Theoretical uncertainties for cosmological first-order phase transitions*, *JHEP* **04** (2021) 055 [[2009.10080](#)].
- [70] P. M. Schicho, T. V. I. Tenkanen and J. Österman, *Robust approach to thermal resummation: Standard Model meets a singlet*, *JHEP* **06** (2021) 130 [[2102.11145](#)].
- [71] P. Athron, C. Balazs, A. Fowlie, L. Morris, G. White and Y. Zhang, *How arbitrary are perturbative calculations of the electroweak phase transition?*, *JHEP* **01** (2023) 050 [[2208.01319](#)].
- [72] O. Gould and C. Xie, *Higher orders for cosmological phase transitions: a global study in a Yukawa model*, *JHEP* **12** (2023) 049 [[2310.02308](#)].
- [73] M. Lewicki, M. Merchand, L. Sagunski, P. Schicho and D. Schmitt, *Impact of theoretical uncertainties on model parameter reconstruction from GW signals sourced by cosmological phase transitions*, [2403.03769](#).
- [74] O. Gould and J. Hirvonen, *Effective field theory approach to thermal bubble nucleation*, *Phys. Rev. D* **104** (2021) 096015 [[2108.04377](#)].
- [75] P. Schicho, T. V. I. Tenkanen and G. White, *Combining thermal resummation and gauge invariance for electroweak phase transition*, *JHEP* **11** (2022) 047 [[2203.04284](#)].
- [76] J. Löfgren, M. J. Ramsey-Musolf, P. Schicho and T. V. I. Tenkanen, *Nucleation at Finite Temperature: A Gauge-Invariant Perturbative Framework*, *Phys. Rev. Lett.* **130** (2023) 251801 [[2112.05472](#)].
- [77] J. Hirvonen, J. Löfgren, M. J. Ramsey-Musolf, P. Schicho and T. V. I. Tenkanen, *Computing the gauge-invariant bubble nucleation rate in finite temperature effective field theory*, *JHEP* **07** (2022) 135 [[2112.08912](#)].

- [78] A. Ekstedt, P. Schicho and T. V. I. Tenkanen, *DRalgo: A package for effective field theory approach for thermal phase transitions*, *Comput. Phys. Commun.* **288** (2023) 108725 [[2205.08815](#)].
- [79] A. Ekstedt, O. Gould and J. Löfgren, *Radiative first-order phase transitions to next-to-next-to-leading order*, *Phys. Rev. D* **106** (2022) 036012 [[2205.07241](#)].
- [80] A. Ekstedt, O. Gould and J. Hirvonen, *BubbleDet: a Python package to compute functional determinants for bubble nucleation*, *JHEP* **12** (2023) 056 [[2308.15652](#)].
- [81] O. Gould and T. V. I. Tenkanen, *Perturbative effective field theory expansions for cosmological phase transitions*, *JHEP* **01** (2024) 048 [[2309.01672](#)].
- [82] L. Giombi and M. Hindmarsh, *General relativistic bubble growth in cosmological phase transitions*, *JCAP* **03** (2024) 059 [[2307.12080](#)].
- [83] Q. Baghi, N. Karnesis, J.-B. Bayle, M. Besançon and H. Inchauspé, *Uncovering gravitational-wave backgrounds from noises of unknown shape with LISA*, *JCAP* **04** (2023) 066 [[2302.12573](#)].
- [84] M. Muratore, J. Gair and L. Speri, *Impact of the noise knowledge uncertainty for the science exploitation of cosmological and astrophysical stochastic gravitational wave background with LISA*, *Phys. Rev. D* **109** (2024) 042001 [[2308.01056](#)].
- [85] F. Pozzoli, R. Buscicchio, C. J. Moore, F. Haardt and A. Sesana, *Weakly parametric approach to stochastic background inference in LISA*, *Phys. Rev. D* **109** (2024) 083029 [[2311.12111](#)].
- [86] G. Boileau, N. Christensen, R. Meyer and N. J. Cornish, *Spectral separation of the stochastic gravitational-wave background for LISA: Observing both cosmological and astrophysical backgrounds*, *Phys. Rev. D* **103** (2021) 103529 [[2011.05055](#)].
- [87] M. Pieroni and E. Barausse, *Foreground cleaning and template-free stochastic background extraction for LISA*, *JCAP* **07** (2020) 021 [[2004.01135](#)].
- [88] G. Boileau, A. Lamberts, N. J. Cornish and R. Meyer, *Spectral separation of the stochastic gravitational-wave background for LISA in the context of a modulated Galactic foreground*, *Mon. Not. Roy. Astron. Soc.* **508** (2021) 803 [[2105.04283](#)].
- [89] M. Lewicki and V. Vaskonen, *Impact of LIGO-Virgo black hole binaries on gravitational wave background searches*, *Eur. Phys. J. C* **83** (2023) 168 [[2111.05847](#)].
- [90] D. Racco and D. Poletti, *Precision cosmology with primordial GW backgrounds in presence of astrophysical foregrounds*, *JCAP* **04** (2023) 054 [[2212.06602](#)].
- [91] J. R. Espinosa, T. Konstandin, J. M. No and G. Servant, *Energy Budget of Cosmological First-order Phase Transitions*, *JCAP* **06** (2010) 028 [[1004.4187](#)].
- [92] E. W. Kolb and M. S. Turner, *The Early Universe*, vol. 69. 1990, [10.1201/9780429492860](#).
- [93] T. Konstandin, *Gravitational radiation from a bulk flow model*, *JCAP* **03** (2018) 047 [[1712.06869](#)].
- [94] D. Bodeker and G. D. Moore, *Can electroweak bubble walls run away?*, *JCAP* **05** (2009) 009 [[0903.4099](#)].
- [95] A. Kosowsky, M. S. Turner and R. Watkins, *Gravitational waves from first order cosmological phase transitions*, *Phys. Rev. Lett.* **69** (1992) 2026.

- [96] D. J. Weir, *Revisiting the envelope approximation: gravitational waves from bubble collisions*, *Phys. Rev. D* **93** (2016) 124037 [[1604.08429](#)].
- [97] R. Jinno and M. Takimoto, *Gravitational waves from bubble collisions: An analytic derivation*, *Phys. Rev. D* **95** (2017) 024009 [[1605.01403](#)].
- [98] H. L. Child and J. T. Giblin, Jr., *Gravitational Radiation from First-Order Phase Transitions*, *JCAP* **10** (2012) 001 [[1207.6408](#)].
- [99] R. Jinno, T. Konstandin and M. Takimoto, *Relativistic bubble collisions—a closer look*, *JCAP* **09** (2019) 035 [[1906.02588](#)].
- [100] R. Jinno and M. Takimoto, *Gravitational waves from bubble dynamics: Beyond the Envelope*, *JCAP* **01** (2019) 060 [[1707.03111](#)].
- [101] D. Bodeker and G. D. Moore, *Electroweak Bubble Wall Speed Limit*, *JCAP* **05** (2017) 025 [[1703.08215](#)].
- [102] S. Höche, J. Kozaczuk, A. J. Long, J. Turner and Y. Wang, *Towards an all-orders calculation of the electroweak bubble wall velocity*, *JCAP* **03** (2021) 009 [[2007.10343](#)].
- [103] A. Azatov, M. Vanvlasselaer and W. Yin, *Baryogenesis via relativistic bubble walls*, *JHEP* **10** (2021) 043 [[2106.14913](#)].
- [104] Y. Gouttenoire, R. Jinno and F. Sala, *Friction pressure on relativistic bubble walls*, *JHEP* **05** (2022) 004 [[2112.07686](#)].
- [105] A. Azatov, G. Barni, R. Petrossian-Byrne and M. Vanvlasselaer, *Quantisation across bubble walls and friction*, *JHEP* **05** (2024) 294 [[2310.06972](#)].
- [106] R. Jinno, H. Seong, M. Takimoto and C. M. Um, *Gravitational waves from first-order phase transitions: Ultra-supercooled transitions and the fate of relativistic shocks*, *JCAP* **10** (2019) 033 [[1905.00899](#)].
- [107] M. Breitbach, J. Kopp, E. Madge, T. Opferkuch and P. Schwaller, *Dark, Cold, and Noisy: Constraining Secluded Hidden Sectors with Gravitational Waves*, *JCAP* **07** (2019) 007 [[1811.11175](#)].
- [108] M. Fairbairn, E. Hardy and A. Wickens, *Hearing without seeing: gravitational waves from hot and cold hidden sectors*, *JHEP* **07** (2019) 044 [[1901.11038](#)].
- [109] C. Caprini, R. Durrer, T. Konstandin and G. Servant, *General Properties of the Gravitational Wave Spectrum from Phase Transitions*, *Phys. Rev. D* **79** (2009) 083519 [[0901.1661](#)].
- [110] A. Kurganov and E. Tadmor, *New High-Resolution Central Schemes for Nonlinear Conservation Laws and Convection–Diffusion Equations*, *J. Comput. Phys.* **160** (2000) 241.
- [111] C. Caprini, R. Jinno, T. Konstandin, A. Roper Pol, H. Rubira and I. Stomberg, *Gravitational waves from decaying sources in strong phase transitions*, [2409.03651](#).
- [112] F. Giese, T. Konstandin and J. van de Vis, *Model-independent energy budget of cosmological first-order phase transitions—A sound argument to go beyond the bag model*, *JCAP* **07** (2020) 057 [[2004.06995](#)].
- [113] F. Giese, T. Konstandin, K. Schmitz and J. van de Vis, *Model-independent energy budget for LISA*, *JCAP* **01** (2021) 072 [[2010.09744](#)].

- [114] R. Banerjee and K. Jedamzik, *The Evolution of cosmic magnetic fields: From the very early universe, to recombination, to the present*, *Phys. Rev. D* **70** (2004) 123003 [[astro-ph/0410032](#)].
- [115] P. A. Seoane et al., *The effect of mission duration on LISA science objectives*, *Gen. Rel. Grav.* **54** (2022) 3 [[2107.09665](#)].
- [116] M. Colpi et al., *LISA Definition Study Report*, [2402.07571](#).
- [117] LISA COSMOLOGY WORKING GROUP collaboration, *Gravitational waves from cosmic strings in LISA: reconstruction pipeline and physics interpretation*, [2405.03740](#).
- [118] LISA COSMOLOGY WORKING GROUP collaboration, *Gravitational waves from inflation in LISA: reconstruction pipeline and physics interpretation*, [2407.04356](#).
- [119] M. Tinto and S. V. Dhurandhar, *Time-delay interferometry*, *Living Rev. Rel.* **24** (2021) 1.
- [120] M. Tinto and J. W. Armstrong, *Cancellation of laser noise in an unequal-arm interferometer detector of gravitational radiation*, *Phys. Rev. D* **59** (1999) 102003.
- [121] T. A. Prince, M. Tinto, S. L. Larson and J. W. Armstrong, *The LISA optimal sensitivity*, *Phys. Rev. D* **66** (2002) 122002 [[gr-qc/0209039](#)].
- [122] D. A. Shaddock, *Operating LISA as a Sagnac interferometer*, *Phys. Rev. D* **69** (2004) 022001 [[gr-qc/0306125](#)].
- [123] D. A. Shaddock, M. Tinto, F. B. Estabrook and J. W. Armstrong, *Data combinations accounting for LISA spacecraft motion*, *Phys. Rev. D* **68** (2003) 061303 [[gr-qc/0307080](#)].
- [124] M. Tinto, F. B. Estabrook and J. W. Armstrong, *Time delay interferometry with moving spacecraft arrays*, *Phys. Rev. D* **69** (2004) 082001 [[gr-qc/0310017](#)].
- [125] M. Vallisneri, *Geometric time delay interferometry*, *Phys. Rev. D* **72** (2005) 042003 [[gr-qc/0504145](#)].
- [126] M. Muratore, D. Vetrugno and S. Vitale, *Revisitation of time delay interferometry combinations that suppress laser noise in LISA*, *Class. Quant. Grav.* **37** (2020) 185019 [[2001.11221](#)].
- [127] M. Muratore, D. Vetrugno, S. Vitale and O. Hartwig, *Time delay interferometry combinations as instrument noise monitors for LISA*, *Phys. Rev. D* **105** (2022) 023009 [[2108.02738](#)].
- [128] O. Hartwig and M. Muratore, *Characterization of time delay interferometry combinations for the LISA instrument noise*, *Phys. Rev. D* **105** (2022) 062006 [[2111.00975](#)].
- [129] O. Hartwig, M. Lilley, M. Muratore and M. Pieroni, *Stochastic gravitational wave background reconstruction for a nonequilateral and unequal-noise LISA constellation*, *Phys. Rev. D* **107** (2023) 123531 [[2303.15929](#)].
- [130] D. Q. Nam, Y. Lemièrre, A. Petiteau, J.-B. Bayle, O. Hartwig, J. Martino et al., *TDI noises transfer functions for LISA*, [2211.02539](#).
- [131] S. Babak, A. Petiteau and M. Hewitson, *LISA Sensitivity and SNR Calculations*, [2108.01167](#).
- [132] E. S. Phinney, *A Practical theorem on gravitational wave backgrounds*, [astro-ph/0108028](#).
- [133] T. Regimbau, *The astrophysical gravitational wave stochastic background*, *Res. Astron. Astrophys.* **11** (2011) 369 [[1101.2762](#)].

- [134] C. P erigois, C. Belczynski, T. Bulik and T. Regimbau, *StarTrack predictions of the stochastic gravitational-wave background from compact binary mergers*, *Phys. Rev. D* **103** (2021) 043002 [[2008.04890](#)].
- [135] S. Babak, C. Caprini, D. G. Figueroa, N. Karnesis, P. Marcoccia, G. Nardini et al., *Stochastic gravitational wave background from stellar origin binary black holes in LISA*, *JCAP* **08** (2023) 034 [[2304.06368](#)].
- [136] L. Lehoucq, I. Dvorkin, R. Srinivasan, C. Pellouin and A. Lamberts, *Astrophysical uncertainties in the gravitational-wave background from stellar-mass compact binary mergers*, *Mon. Not. Roy. Astron. Soc.* **526** (2023) 4378 [[2306.09861](#)].
- [137] KAGRA, VIRGO, LIGO SCIENTIFIC collaboration, *Population of Merging Compact Binaries Inferred Using Gravitational Waves through GWTC-3*, *Phys. Rev. X* **13** (2023) 011048 [[2111.03634](#)].
- [138] S. Nissanke, M. Vallisneri, G. Nelemans and T. A. Prince, *Gravitational-wave emission from compact Galactic binaries*, *Astrophys. J.* **758** (2012) 131 [[1201.4613](#)].
- [139] N. Karnesis, S. Babak, M. Pieroni, N. Cornish and T. Littenberg, *Characterization of the stochastic signal originating from compact binary populations as measured by LISA*, *Phys. Rev. D* **104** (2021) 043019 [[2103.14598](#)].
- [140] J. R. Bond, A. H. Jaffe and L. E. Knox, *Radical compression of cosmic microwave background data*, *Astrophys. J.* **533** (2000) 19 [[astro-ph/9808264](#)].
- [141] J. L. Sievers et al., *Cosmological parameters from Cosmic Background Imager observations and comparisons with BOOMERANG, DASI, and MAXIMA*, *Astrophys. J.* **591** (2003) 599 [[astro-ph/0205387](#)].
- [142] WMAP collaboration, *First year Wilkinson Microwave Anisotropy Probe (WMAP) observations: Parameter estimation methodology*, *Astrophys. J. Suppl.* **148** (2003) 195 [[astro-ph/0302218](#)].
- [143] S. Hamimeche and A. Lewis, *Likelihood Analysis of CMB Temperature and Polarization Power Spectra*, *Phys. Rev. D* **77** (2008) 103013 [[0801.0554](#)].
- [144] W. J. Handley, M. P. Hobson and A. N. Lasenby, *polychord: next-generation nested sampling*, *Mon. Not. Roy. Astron. Soc.* **453** (2015) 4385 [[1506.00171](#)].
- [145] W. J. Handley, M. P. Hobson and A. N. Lasenby, *PolyChord: nested sampling for cosmology*, *Mon. Not. Roy. Astron. Soc.* **450** (2015) L61 [[1502.01856](#)].
- [146] J. Torrado and A. Lewis, *Cobaya: Code for Bayesian Analysis of hierarchical physical models*, *JCAP* **05** (2021) 057 [[2005.05290](#)].
- [147] A. Lewis, *GetDist: a Python package for analysing Monte Carlo samples*, [1910.13970](#).
- [148] J. D. Romano and N. J. Cornish, *Detection methods for stochastic gravitational-wave backgrounds: a unified treatment*, *Living Rev. Rel.* **20** (2017) 2 [[1608.06889](#)].
- [149] B. Sathyaprakash et al., *Scientific Objectives of Einstein Telescope*, *Class. Quant. Grav.* **29** (2012) 124013 [[1206.0331](#)].
- [150] G. Janssen et al., *Gravitational wave astronomy with the SKA*, *PoS AASKA14* (2015) 037 [[1501.00127](#)].
- [151] S. Hild et al., *Sensitivity Studies for Third-Generation Gravitational Wave Observatories*, *Class. Quant. Grav.* **28** (2011) 094013 [[1012.0908](#)].

- [152] A. Weltman et al., *Fundamental physics with the Square Kilometre Array*, *Publ. Astron. Soc. Austral.* **37** (2020) e002 [[1810.02680](#)].
- [153] C. L. Wainwright, *CosmoTransitions: Computing Cosmological Phase Transition Temperatures and Bubble Profiles with Multiple Fields*, *Comput. Phys. Commun.* **183** (2012) 2006 [[1109.4189](#)].
- [154] P. Basler and M. Mühlleitner, *BSMPT (Beyond the Standard Model Phase Transitions): A tool for the electroweak phase transition in extended Higgs sectors*, *Comput. Phys. Commun.* **237** (2019) 62 [[1803.02846](#)].
- [155] P. Athron, C. Balázs, A. Fowlie and Y. Zhang, *PhaseTracer: tracing cosmological phases and calculating transition properties*, *Eur. Phys. J. C* **80** (2020) 567 [[2003.02859](#)].
- [156] A. D. Linde, *Fate of the False Vacuum at Finite Temperature: Theory and Applications*, *Phys. Lett. B* **100** (1981) 37.
- [157] A. D. Linde, *Decay of the False Vacuum at Finite Temperature*, *Nucl. Phys. B* **216** (1983) 421.
- [158] A. H. Guth and E. J. Weinberg, *Could the Universe Have Recovered from a Slow First Order Phase Transition?*, *Nucl. Phys. B* **212** (1983) 321.
- [159] B. Laurent and J. M. Cline, *Fluid equations for fast-moving electroweak bubble walls*, *Phys. Rev. D* **102** (2020) 063516 [[2007.10935](#)].
- [160] J. M. Cline, A. Friedlander, D.-M. He, K. Kainulainen, B. Laurent and D. Tucker-Smith, *Baryogenesis and gravity waves from a UV-completed electroweak phase transition*, *Phys. Rev. D* **103** (2021) 123529 [[2102.12490](#)].
- [161] M. Lewicki, M. Merchand and M. Zych, *Electroweak bubble wall expansion: gravitational waves and baryogenesis in Standard Model-like thermal plasma*, *JHEP* **02** (2022) 017 [[2111.02393](#)].
- [162] B. Laurent and J. M. Cline, *First principles determination of bubble wall velocity*, *Phys. Rev. D* **106** (2022) 023501 [[2204.13120](#)].
- [163] J. Ellis, M. Lewicki, M. Merchand, J. M. No and M. Zych, *The scalar singlet extension of the Standard Model: gravitational waves versus baryogenesis*, *JHEP* **01** (2023) 093 [[2210.16305](#)].
- [164] J. McDonald, *Electroweak baryogenesis and dark matter via a gauge singlet scalar*, *Phys. Lett. B* **323** (1994) 339.
- [165] J. R. Espinosa and M. Quiros, *The Electroweak phase transition with a singlet*, *Phys. Lett. B* **305** (1993) 98 [[hep-ph/9301285](#)].
- [166] J. R. Espinosa and M. Quiros, *Novel Effects in Electroweak Breaking from a Hidden Sector*, *Phys. Rev. D* **76** (2007) 076004 [[hep-ph/0701145](#)].
- [167] S. Profumo, M. J. Ramsey-Musolf and G. Shaughnessy, *Singlet Higgs phenomenology and the electroweak phase transition*, *JHEP* **08** (2007) 010 [[0705.2425](#)].
- [168] J. R. Espinosa, T. Konstandin and F. Riva, *Strong Electroweak Phase Transitions in the Standard Model with a Singlet*, *Nucl. Phys. B* **854** (2012) 592 [[1107.5441](#)].
- [169] V. Barger, D. J. H. Chung, A. J. Long and L.-T. Wang, *Strongly First Order Phase Transitions Near an Enhanced Discrete Symmetry Point*, *Phys. Lett. B* **710** (2012) 1 [[1112.5460](#)].

- [170] J. M. Cline and K. Kainulainen, *Electroweak baryogenesis and dark matter from a singlet Higgs*, *JCAP* **01** (2013) 012 [[1210.4196](#)].
- [171] T. Alanne, K. Tuominen and V. Vaskonen, *Strong phase transition, dark matter and vacuum stability from simple hidden sectors*, *Nucl. Phys. B* **889** (2014) 692 [[1407.0688](#)].
- [172] D. Curtin, P. Meade and C.-T. Yu, *Testing Electroweak Baryogenesis with Future Colliders*, *JHEP* **11** (2014) 127 [[1409.0005](#)].
- [173] V. Vaskonen, *Electroweak baryogenesis and gravitational waves from a real scalar singlet*, *Phys. Rev. D* **95** (2017) 123515 [[1611.02073](#)].
- [174] G. Kurup and M. Perelstein, *Dynamics of Electroweak Phase Transition In Singlet-Scalar Extension of the Standard Model*, *Phys. Rev. D* **96** (2017) 015036 [[1704.03381](#)].
- [175] A. Beniwal, M. Lewicki, J. D. Wells, M. White and A. G. Williams, *Gravitational wave, collider and dark matter signals from a scalar singlet electroweak baryogenesis*, *JHEP* **08** (2017) 108 [[1702.06124](#)].
- [176] L. Niemi, P. Schicho and T. V. I. Tenkanen, *Singlet-assisted electroweak phase transition at two loops*, *Phys. Rev. D* **103** (2021) 115035 [[2103.07467](#)].
- [177] S. Blasi and A. Mariotti, *Domain Walls Seeding the Electroweak Phase Transition*, *Phys. Rev. Lett.* **129** (2022) 261303 [[2203.16450](#)].
- [178] A. Beniwal, M. Lewicki, M. White and A. G. Williams, *Gravitational waves and electroweak baryogenesis in a global study of the extended scalar singlet model*, *JHEP* **02** (2019) 183 [[1810.02380](#)].
- [179] A. Azatov, G. Barni, S. Chakraborty, M. Vanvlasselaer and W. Yin, *Ultra-relativistic bubbles from the simplest Higgs portal and their cosmological consequences*, *JHEP* **10** (2022) 017 [[2207.02230](#)].
- [180] S. R. Hinton, *ChainConsumer*, *The Journal of Open Source Software* **1** (2016) 00045.
- [181] N. Craig, H. K. Lou, M. McCullough and A. Thalappilil, *The Higgs Portal Above Threshold*, *JHEP* **02** (2016) 127 [[1412.0258](#)].
- [182] B. Allen and J. D. Romano, *Detecting a stochastic background of gravitational radiation: Signal processing strategies and sensitivities*, *Phys. Rev. D* **59** (1999) 102001 [[gr-qc/9710117](#)].
- [183] S. Iso, N. Okada and Y. Orikasa, *Classically conformal B – L extended Standard Model*, *Phys. Lett. B* **676** (2009) 81 [[0902.4050](#)].
- [184] S. Iso, N. Okada and Y. Orikasa, *The minimal B-L model naturally realized at TeV scale*, *Phys. Rev. D* **80** (2009) 115007 [[0909.0128](#)].
- [185] R. Jinno and M. Takimoto, *Probing a classically conformal B-L model with gravitational waves*, *Phys. Rev. D* **95** (2017) 015020 [[1604.05035](#)].
- [186] S. Iso, P. D. Serpico and K. Shimada, *QCD-Electroweak First-Order Phase Transition in a Supercooled Universe*, *Phys. Rev. Lett.* **119** (2017) 141301 [[1704.04955](#)].
- [187] C. Marzo, L. Marzola and V. Vaskonen, *Phase transition and vacuum stability in the classically conformal B–L model*, *Eur. Phys. J. C* **79** (2019) 601 [[1811.11169](#)].
- [188] J. Ellis, M. Lewicki, J. M. No and V. Vaskonen, *Gravitational wave energy budget in strongly supercooled phase transitions*, *JCAP* **06** (2019) 024 [[1903.09642](#)].

- [189] L. Sagunski, P. Schicho and D. Schmitt, *Supercool exit: Gravitational waves from QCD-triggered conformal symmetry breaking*, *Phys. Rev. D* **107** (2023) 123512 [[2303.02450](#)].
- [190] M. Escudero, S. J. Witte and N. Rius, *The dispirited case of gauged $U(1)_{B-L}$ dark matter*, *JHEP* **08** (2018) 190 [[1806.02823](#)].
- [191] J. Jaeckel, V. V. Khoze and M. Spannowsky, *Hearing the signal of dark sectors with gravitational wave detectors*, *Phys. Rev. D* **94** (2016) 103519 [[1602.03901](#)].
- [192] A. Dasgupta, P. S. B. Dev, A. Ghoshal and A. Mazumdar, *Gravitational wave pathway to testable leptogenesis*, *Phys. Rev. D* **106** (2022) 075027 [[2206.07032](#)].
- [193] FCC collaboration, *FCC-hh: The Hadron Collider: Future Circular Collider Conceptual Design Report Volume 3*, *Eur. Phys. J. ST* **228** (2019) 755.
- [194] T. Robson, N. J. Cornish and C. Liu, *The construction and use of LISA sensitivity curves*, *Class. Quant. Grav.* **36** (2019) 105011 [[1803.01944](#)].